Supplementary Information for
Nonlinear cascaded quantum network with giant emitters

Xin Wang[1,2], Jia-Qi Li[1], Zhi-Hai Wang[3], Anton Frisk Kockum[4], Lei Du[4], Tao Liu[5], and Franco Nori[2,6]

[1] *Shaanxi Province Key Laboratory of Quantum Information and Quantum Optoelectronic Devices, School of Physics, Xi'an Jiaotong University, Xi'an 710049, People's Republic of China*

[2] *Center for Quantum Computing, RIKEN, Wako-shi, Saitama 351-0198, Japan*

[3] *Center for Quantum Sciences and School of Physics, Northeast Normal University, Changchun 130024, People's Republic of China*

[4] *Department of Microtechnology and Nanoscience, Chalmers University of Technology, 41296 Gothenburg, Sweden*

[5] *School of Physics and Optoelectronics, South China University of Technology, Guangzhou 510640, People's Republic of China*

[6] *Physics Department, The University of Michigan, Ann Arbor, Michigan 48109-1040, USA*

In Sec. Supplementary Note 1, we derive the dispersion relation and wave function of a doublon (i.e., a correlated photon pair) in a waveguide with on-site photon-photon interactions. In Sec. Supplementary Note 2, we derive the analytical solutions for the spontaneous decay rate and explain the mechanism for chiral emission. We also demonstrate how the geometric structure, the encoded phases, and frequency mismatch affect the chiral behavior of the giant-emitter pair (GEP). In Sec. Supplementary Note 3, we demonstrate two applications of our proposal: generating stationary four-body entangled states between remote GEPs and modulating the coupling strength to realize the state transfer between remote GEPs. In Sec. Supplementary Note 4, we demonstrate that our proposal can yield directional routing of $\mathcal{N}$ correlated photons, beyond photon pairs.

CONTENTS

Supplementary Note 1. DOUBLON SPECTRUM

We consider a waveguide composed of an array of coupled cavities with nearest-neighbor coupling strength J and nonlinear potential U. When $U > 0$ ($U < 0$), the photon-photon interaction is repulsive (attractive). The resonance frequency of the cavities is set to ω_c. For convenience, we set the length of one unit site to $l_0 = 1$. In a frame rotating with ω_c, the waveguide Hamiltonian is then

$$\begin{gathered} H_\mathrm{w} = H_0 + H_U, \\ H_0 = \sum_n -J\left(a_n^\dagger a_{n+1} + \mathrm{H.c.}\right), \quad H_U = \sum_n \frac{U}{2} a_n^\dagger a_n^\dagger a_n a_n. \end{gathered} \tag{S1}$$

In the two-photon subspace, the waveguide state is expressed as [S1–S3]

$$|\Psi\rangle = \frac{1}{\sqrt{2}} \sum_{m,n=1}^{N} \psi_{m,n} a_m^\dagger a_n^\dagger |\mathrm{vac}\rangle, \tag{S2}$$

where $\psi_{m,n}$ is the probability amplitude of two photons being excited, one at position m and one at position n. By substituting $|\Psi\rangle$ and H_w into the Schrödinger equation, we obtain

$$U\delta_{m,n}\psi_{m,n} - J\sum_\pm (\psi_{m\pm1,n} + \psi_{m,n\pm1}) = E\psi_{m,n}. \tag{S3}$$

Written in the center-of-mass and relative coordinates, i.e., $x_\mathrm{c} = (m+n)/2$ and $r_\mathrm{d} = m - n$, Eq. (S3) becomes

$$U\delta_{r,0}\psi_{x_\mathrm{c},r_\mathrm{d}} - J\sum_\pm \left(\psi_{x_\mathrm{c}+\frac{1}{2},r_\mathrm{d}\pm1} + \psi_{x_\mathrm{c}-\frac{1}{2},r_\mathrm{d}\pm1}\right) = E\psi_{x_\mathrm{c},r_\mathrm{d}}. \tag{S4}$$

The wave function can be expressed in terms of a separable solution

$$\psi_{x_\mathrm{c},r_\mathrm{d}} = e^{iKx_\mathrm{c}} u_K(r_\mathrm{d}), \tag{S5}$$

where K is the center-of-mass quasi-momentum. The discrete eigen-equation is then transformed into

$$-2J\cos\left(\frac{K}{2}\right)[u_K(r_\mathrm{d}+1) + u_K(r_\mathrm{d}-1)] + U\delta_{r_\mathrm{d},0}u_K(r_\mathrm{d}) = Eu_K(r_\mathrm{d}). \tag{S6}$$

In the absence of U, the unperturbed Green's function is [S1]

$$(E - H_0)G_K^0(E, r_\mathrm{d}) = \delta_{r_\mathrm{d},0}. \tag{S7}$$

Applying the Fourier transform to both sides of Eq. (S7), it becomes

$$\frac{1}{2\pi}\int dq\ (E - H_0)G_K^0(E,q)e^{iqr_\mathrm{d}} = \frac{1}{2\pi}\int dq\ e^{iqr_\mathrm{d}}, \tag{S8}$$

where $G_K^0(E, r_\mathrm{d}) = \frac{1}{2\pi}\int dq\ G_K^0(E,q)e^{iqr_\mathrm{d}}$. Note that e^{iqr_d} is an eigenvector of H_0, i.e.,

$$H_0\ e^{iqr_\mathrm{d}} = \left[-4J\cos\left(\frac{K}{2}\right)\cos q\right]\ e^{iqr_\mathrm{d}}. \tag{S9}$$

Therefore, G_K^0 is derived as

$$(E - H_0)G_K^0(E,q) = 1 \longrightarrow G_K^0(E,q) = \frac{1}{E - H_0} = \frac{1}{E + 4J\cos\left(\frac{K}{2}\right)\cos q}. \tag{S10}$$

The full Green's function $G_K(E, r_\mathrm{d})$ is obtained via the Lippmann-Schwinger equation:

$$\begin{aligned} G_K(E, r_\mathrm{d}) &= G_K^0(E, r_\mathrm{d}) + \int dr_\mathrm{d}'\ G_K^0(E, r_\mathrm{d} - r_\mathrm{d}')V(r_\mathrm{d}')G_K(E, r_\mathrm{d}') \\ &= G_K^0(E, r_\mathrm{d}) + G_K^0(E, r_\mathrm{d})UG_K(E, r_\mathrm{d} = 0) \\ &= G_K^0(E, r_\mathrm{d}) + G_K^0(E, r_\mathrm{d})\frac{G_K^0(E, r_\mathrm{d} = 0)U}{1 - G_K^0(E, r_\mathrm{d} = 0)U}. \end{aligned} \tag{S11}$$

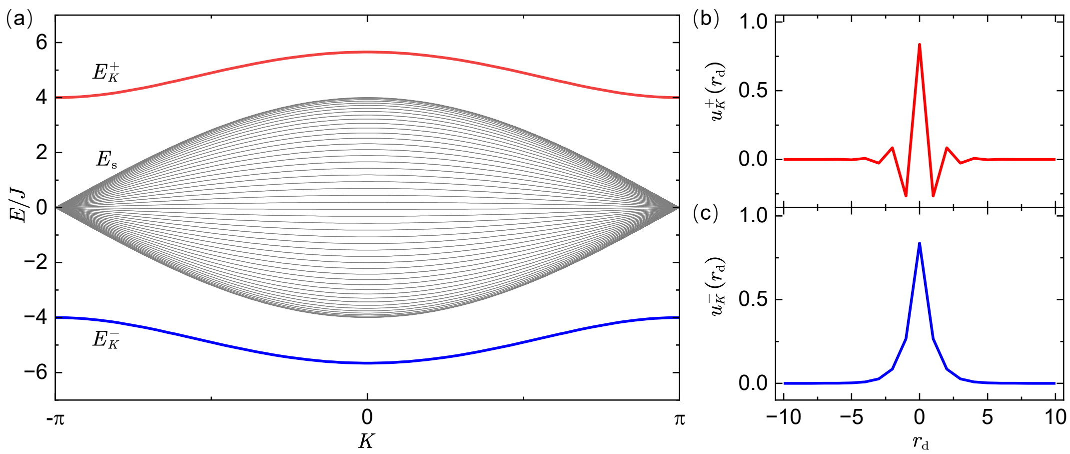

Figure S1. **Doublon spectrum and wavefunctions.** (a) Spectrum of the two-photon subspace. The bound states $E_K^{\pm}$ are given by Eqs. (S14) (red solid curve) and (S15) (blue solid curve); while the scatter state is given by Eq. (S20) (gray curves). (b, c) Wavefunctions $u^{\pm}K(r_\mathrm{d})$ of the bound states at $K = \pi/2$, given by Eqs. (S16) and (S17). The superscript $\pm$ denotes the sign of the interaction U.

where $V(r_\mathrm{d}) = U\delta_{r_\mathrm{d},0}$ and the first term corresponds to the eigensolution of the non-interacting Hamiltonian H_0, representing the scattering state.

Here, we focus on the doublon state, where two photons are bound together in the presence of the nonlinear potential U. Therefore, we require [S1, S2]

$$1 - G_K^0(E, r_\mathrm{d} = 0)U = 0, \tag{S12}$$

$$\frac{1}{U} = G_K^0 = \int dq \, \frac{1}{E + 4J\cos\left(\frac{K}{2}\right)\cos q}. \tag{S13}$$

Finally, the dispersion relation of the doublon state is derived by solving Eq. (S13), yielding

$$U > 0, \quad E_K = \sqrt{U^2 + 16J^2\cos^2(K/2)}, \tag{S14}$$

$$U < 0, \quad E_K = -\sqrt{U^2 + 16J^2\cos^2(K/2)}. \tag{S15}$$

Note that $E_K(U < 0) = -E_K(U > 0)$. We plot the dispersion relation E_K in Fig. 1(c) in the main text by assuming $U < 0$. The wave function for mode K is written as

$$\begin{aligned} u_K(r_\mathrm{d}) &= \frac{G_K^0(E, r_\mathrm{d} = 0)U}{1 - G_K^0(E, r_\mathrm{d} = 0)U} G_K^0(E, r_\mathrm{d}) \\ &= \frac{G_K^0(E, r_\mathrm{d} = 0)U}{1 - G_K^0(E, r_\mathrm{d} = 0)U} \frac{1}{2\pi} \int dq \, \frac{e^{iqr_\mathrm{d}}}{E + 4J\cos\left(\frac{K}{2}\right)\cos q}. \end{aligned}$$

Then, the wavefunction is written as [S1–S3]

$$U > 0, \quad u_K(r_\mathrm{d}) = u_0(-1)^{|r_\mathrm{d}|}\exp\left[-\frac{|r_\mathrm{d}|}{L_u(K)}\right], \tag{S16}$$

$$U < 0, \quad u_K(r_\mathrm{d}) = u_0\exp\left[-\frac{|r_\mathrm{d}|}{L_u(K)}\right], \tag{S17}$$

where u_0 is a normalization factor and the decay length for two-photon correlations in space is

$$L_u(K) = -\left[\ln\left(\frac{\sqrt{U^2 + 16J_K^2} - |U|}{4J_K}\right)\right]^{-1}, \tag{S18}$$

with $J_K = J\cos(K/2)$. Note that $L_u(K)$ rapidly decreases when increasing the nonlinear parameter U. Eventually, the wave function of the doublon state is written as

$$\Psi_{\mathrm{d}} = \frac{1}{\sqrt{2}} \sum_{m,n} e^{iK\frac{m+n}{2}} u_K(m-n). \tag{S19}$$

In Fig. S1, we plot the band structure $E_K^{\pm}$ versus K and the wavefunction $u_K^{\pm}(r_{\mathrm{d}})$ versus r_{d} at $K = \pi/2$. The superscript $\pm$ corresponds to the sign of the interaction U. The scattering state is plotted for reference [S3]

$$E_{\mathrm{s}} = -4J\cos(K/2)\cos(q), \tag{S20}$$

with relative momentum q.

We focus on the case $U < 0$ throughout the article and a discussion of how $U > 0$ affects these conclusions follows in the Sec. Supplementary Note 2 D.

Supplementary Note 2. CHIRAL EMISSION OF CORRELATED PHOTON PAIRS

A. Effective transitions between bath and GEP

As depicted in Fig. 1(a) in the main text, we consider a giant-emitter pair (GEP) interacting with the nonlinear waveguide at points $n_{1(2)}^{1/\mathrm{r}}$ with coupling phases $\phi_{1(2)}^{1/\mathrm{r}}$. The frequencies of the two emitters are assumed to lie within the doublon spectrum, which leads to the supercorrelated emission from the GEP [S2]. In the following, we focus on the evolution dynamics of the GEP and discuss the influence of the GEP geometric layout and the coupling phases on the chiral emission.

By using $a_n^\dagger = 1/\sqrt{N}\sum_k e^{-ikn} a_k^\dagger$, the Hamiltonian of the whole system is written as

$$H = \sum_s \omega_s |\Psi_s\rangle\langle\Psi_s| + \sum_K E_K \mathcal{D}_K^\dagger \mathcal{D}_K + \frac{\omega_{\mathrm{e}}}{2}\sum_{m=1}^{2} \sigma_m^z + H_{\mathrm{int}}, \tag{S21}$$

$$H_{\mathrm{int}} = \sum_{m=1}^{2} \frac{g}{\sqrt{N}} \left(\sum_k e^{-ikn_m^{\mathrm{l}}} e^{i\phi_m^{\mathrm{l}}} \sigma_m^- a_k^\dagger + \sum_k e^{-ikn_m^{\mathrm{r}}} e^{i\phi_m^{\mathrm{r}}} \sigma_m^- a_k^\dagger \right) + \mathrm{H.c.}, \tag{S22}$$

where $|\Psi_s\rangle$ is the wave function of the scattering state with eigenenergy ω_s and $\mathcal{D}_K^\dagger$ is the creation operator for a doublon state with wave vector K, i.e., $|\Psi_{\mathrm{d}}\rangle = \mathcal{D}_K^\dagger |\mathrm{vac}\rangle$. As depicted in Fig. 1(b) in the main text, we set $2\omega_{\mathrm{e}}$ to be inside the continuous doublon spectrum, while being well separated from the two-photon scattering state. Therefore, we can neglect the scatting states $|\Psi_s\rangle$ in the following discussion. The state of the system can be expanded as

$$|\psi(t)\rangle = \left[c_{\mathrm{e}}(t)\sigma_1^+\sigma_2^+ + \sum_K c_K(t)\mathcal{D}_K^\dagger + \sum_{m=1}^{2}\sum_k c_{mk}\sigma_m^+ a_k^\dagger \right] |g, g, \mathrm{vac}\rangle, \tag{S23}$$

where $c_{\mathrm{e}}(t)$ is the probability amplitude for the two giant emitters simultaneously being in their excited states, $c_K(t)$ is the probability amplitude for the doublon mode K being excited, and c_{mk} denotes the probability amplitude for both the mth giant emitter and the single-photon mode k being excited. By substituting $|\psi(t)\rangle$ from Eq. (S23) and H from Eq. (S21) into the Schrödinger equation, we obtain the evolution equations

$$i\dot{c}_{\mathrm{e}}(t) = \frac{1}{\sqrt{N}} \sum_{m=1}^{2} \sum_k g\left(e^{ikn_m^{\mathrm{l}}} e^{-i\phi_m^{\mathrm{l}}} + e^{ikn_m^{\mathrm{r}}} e^{-i\phi_m^{\mathrm{r}}} \right) c_{m'k}(t), \tag{S24}$$

$$i\dot{c}_{mk}(t) = \delta_k c_{mk}(t) + \sum_{\tau=\mathrm{l,r}} \frac{g}{\sqrt{N}} e^{-ikn_{m'}^{\tau}} e^{i\phi_{m'}^{\tau}} c_{\mathrm{e}}(t) + \sum_{\sigma=\mathrm{l,r}} \sum_K g e^{-i\phi_m^{\sigma}} M(k, n_m^{\sigma}, K) c_K(t), \tag{S25}$$

$$i\dot{c}_K(t) = \Delta_K c_K(t) + \sum_{m=1}^{2}\sum_k g\left[e^{i\phi_m^{\mathrm{l}}} M^*\big(k, n_m^{\mathrm{l}}, K\big) + e^{i\phi_m^{\mathrm{r}}} M^*\big(k, n_m^{\mathrm{r}}, K\big) \right] c_{mk}(t), \tag{S26}$$

where $\delta_k = \omega_k - \Delta_{\rm e}$, with $\Delta_{\rm e} = \omega_{\rm e} - \omega_{\rm c}$, $\omega_k = -2J\cos k$, and $\Delta_K = E_K - 2\Delta_{\rm e}$. The notations m and m' represent different giant emitters, i.e., $(m, m') = (1, 2)$ / $(2, 1)$, and $\tau, \sigma =$ l,r represent the left/right interaction points of each giant emitter. The coupling-matrix element $M(k, n, K) = \langle{\rm vac}|a_k a_n \mathcal{D}_K^\dagger|{\rm vac}\rangle$ is

$$M(k,n,K) = \langle{\rm vac}|\frac{1}{N}\sum_m e^{-ikm} a_m a_n \frac{1}{\sqrt{2}}\sum_{m',n'} e^{iK(m'+n')/2} u_K(m'-n') a_{m'}^\dagger a_{n'}^\dagger |{\rm vac}\rangle, \tag{S27}$$

which describes the process of creating a doublon state with wave vector K by annihilating a photon with wave vector k and a photon at position n [S2].

In our discussion, we assume that $\Delta_{\rm e}$ is significantly detuned from the single-photon scattering state. Consequently, the single-photon transitions c_{mk} are suppressed, which enables us to adiabatically eliminate c_{mk} by assuming $\dot{c}_{mk}(t) = 0$, i.e.,

$$c_{mk}(t) \simeq -\left[\sum_{\tau={\rm l,r}} \frac{g}{\delta_k\sqrt{N}} e^{-ikn_{m'}^\tau} e^{i\phi_{m'}^\tau} c_{\rm e}(t) + \sum_K \frac{g}{\delta_k} e^{-i\phi_m^\tau} M(k, n_m^\tau, K) c_K(t)\right]. \tag{S28}$$

By substituting Eq. (S28) into Eq. (S24) and Eq. (S26), respectively, the evolution equations then become

$$i\dot{c}_{\rm e}(t) = -\frac{g^2}{J\sqrt{N_{\rm c}}}\sum_K F_K^* c_K(t), \tag{S29}$$

$$i\dot{c}_K(t) = \Delta_K c_K(t) - \frac{g^2}{J\sqrt{N_{\rm c}}} F_K c_{\rm e}(t), \tag{S30}$$

where we have neglected the Stark shift and the interactions between different doublon modes, the contributions of which to supercorrelated decay is weak (see discussions in Ref. [S2]). Note that the coefficient F_K is

$$F_K = \sum_{m=1}^{2}\sum_k \frac{J}{\delta_k}\left[e^{i\phi_m^{\rm l}} e^{-ikn_m^{\rm l}} + e^{i\phi_m^{\rm r}} e^{-ikn_m^{\rm r}}\right]\left[e^{i\phi_{m'}^{\rm l}} M^*\big(k, n_{m'}^{\rm l}, K\big) + e^{i\phi_{m'}^{\rm r}} M^*(k, n_{m'}^{\rm r}, K)\right] \tag{S31}$$

$$= \sum_{m=1}^{2}\sum_k \frac{J}{\delta_k}\left[\sum_{\tau={\rm l,r}} e^{i\phi_m^\tau} e^{-ikn_m^\tau}\right]\left[\sum_{\sigma={\rm l,r}} e^{i\phi_{m'}^\sigma} M^*(k, n_{m'}^\sigma, K)\right]. \tag{S32}$$

By integrating Eq. (S30), we obtain

$$c_K(t) \simeq i\frac{g^2}{J\sqrt{N_{\rm c}}} F_K \int_0^t dt'\ c_{\rm e}(t') e^{-i\Delta_K(t-t')}, \tag{S33}$$

$$\dot{c}_{\rm e}(t) = -\frac{g^4}{J^2 N_{\rm c}}\sum_K F_K^* F_K \int_0^t dt'\ c_{\rm e}(t') e^{-i\Delta_K(t-t')}. \tag{S34}$$

B. Mechanism of the correlated directional emission

We now focus on the interference of the dynamics. By substituting Eq. (S27) into Eq. (S32), we obtain

$$F_K = \sum_{m=1,2}\sum_{\tau,\sigma={\rm l,r}}\sum_{x_1,x_2}\left[\frac{\sqrt{2}}{N}\sum_k \frac{J}{\delta_k} e^{ik(x_1-n_m^\tau)} e^{i\phi_m^\tau}\right]\left[\delta_{x_2,n_{m'}^\sigma} e^{i\phi_{m'}^\sigma}\right]\left[e^{-iK(x_1+x_2)/2} u_K(x_1-x_2)\right], \tag{S35}$$

which represents the following process: emitter m excites a single-photon intermediate state spreading around the point n_m^τ with an encoded phase ϕ_m^τ. Meanwhile, emitter m' emits another photon at point $n_{m'}^\sigma$ with encoded phase $\phi_{m'}^\sigma$. The summation over x_1, x_2 gives the overlap between the wave function of this photon pair $(n_m^\tau, n_{m'}^\sigma)$ and the doublon state K, which is proportional to the transition rate. Here, the τ and σ denote the coupling points of different emitters.

The expression for F_K is simplified as

$$F_K = \sum_{\tau,\sigma={\rm l,r}}\sum_k L_{k,K}\cos[(k-K/2)(n_1^\tau - n_2^\sigma)] e^{-iK\frac{n_1^\tau+n_2^\sigma}{2}} e^{i\phi_1^\tau} e^{i\phi_2^\sigma}, \tag{S36}$$

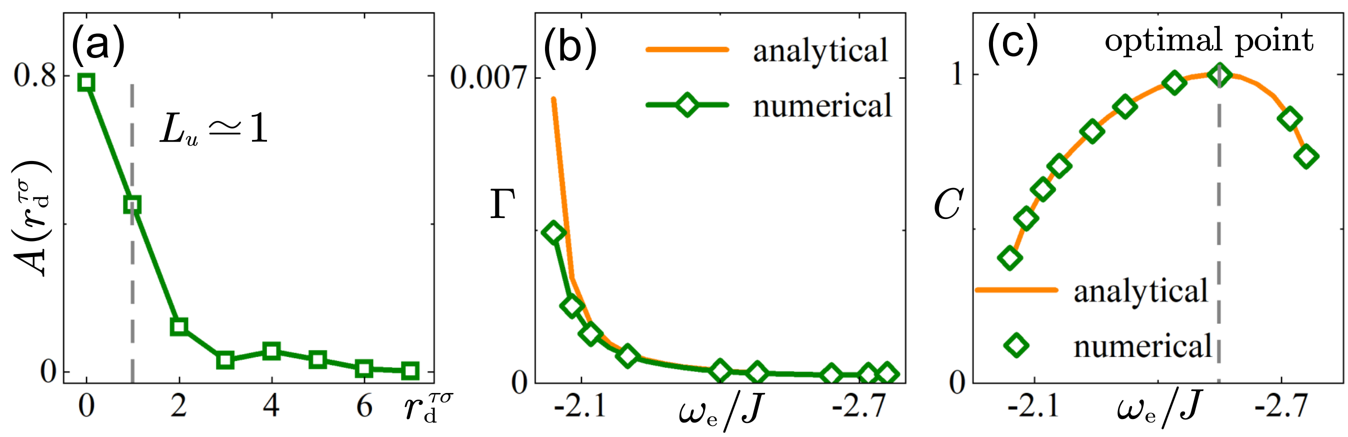

Figure S2. **The emitter dynamic parameters.** (a) The amplitude $A(r_{\rm d}^{\tau\sigma})$ of $\vec{e}_{\tau\sigma}$ as a function of the distance $r_{\rm d}^{\tau\sigma} = |n_1^\tau - n_2^\sigma|$ between two coupling points. The two-photon correlation length for the doublon wavefunction of resonant mode K_r is $L_u(K_r)$. When $r_{\rm d}^{\tau\sigma} > L_u(K_r)$, $A(r_{\rm d}^{\tau\sigma}) \simeq 0$. The gray dashed line denotes the approximate value of $L_u \simeq 1$. (b) The decay rate and (c) the chiral factor as a function of the frequency $\Delta_{\rm e} = \omega_{\rm e} - \omega_{\rm c}$ of the emitters, plotted from numerical simulations (green diamonds); analytical results (orange curve) are given by Eq. (S45). The gray dashed line denotes the optimal frequency. The parameters are the same as those in Fig. 2 of the main text.

where

$$L_{k,K} = \frac{2\sqrt{2}J}{N\delta_k} \sum_m e^{-i(k-K/2)m} u_K(m) \tag{S37}$$

denotes the contribution of each mode k to exciting the doublon mode K. Note that F_K contains four terms, i.e., four decay channels

$$(\tau,\ \sigma)\ =\ (l,\ l),\ (l,\ r),\ (r,\ l),\ (r,\ r), \tag{S38}$$

which correspond to the processes that the GEP emits the photon pair via the coupling points n_1^τ and n_2^σ. Therefore, interference effects exist among these channels. To reveal these effects, we rewrite Eq. (S36) as

$$F_K = \sum_{\tau,\sigma} \vec{e}_{\tau\sigma}, \tag{S39}$$

$$\vec{e}_{\tau\sigma} = A_{\tau\sigma} e^{i\phi_1^\tau} e^{i\phi_2^\sigma} e^{-i\Phi_{\rm d}}, \tag{S40}$$

where $\Phi_{\rm d} = K x_{\rm c}^{\tau\sigma} = K(n_1^\tau + n_2^\sigma)/2$. Here,

$$A_{\tau\sigma} = A(r_{\rm d}^{\tau\sigma}) = \sum_k L_{k,K} \cos[(k - K/2) r_{\rm d}^{\tau\sigma}] \tag{S41}$$

with $r_{\rm d}^{\tau\sigma} = |n_1^\tau - n_\sigma^\tau|$. The physical mechanism represented by $f_K(n_1^\tau, n_2^\sigma)$ has been discussed in connection with Eq. (7) in the main text. We plot $A(r_{\rm d}^{\tau\sigma})$ as a function of $r_{\rm d}^{\tau\sigma}$ in Fig. S2(a). When increasing $r_{\rm d}^{\tau\sigma}$, $A(r_{\rm d}^{\tau\sigma})$, which is the overlap area between the wave function of the photon pair (n_1^τ, n_2^σ) and the doublon state K, rapidly decreases. When $r_{\rm d}^{\tau\sigma}$ is larger than the two-photon correlation length $L_u(K_r)$, $A(r_{\rm d}^{\tau\sigma}) \simeq 0$, indicating that the contribution of the channel (τ, σ) almost vanishes.

Under the Markovian approximation, the dynamics are approximately determined by the interactions between the GEP and the modes around $\pm K_r$. The resonant mode is $E_{\pm K_r} = 2\Delta_{\rm e}$. We approximate F_K as a constant F_{K_r} because only the modes around $\pm K_r$ are significantly excited. Therefore,

$$\sum_K |F_K|^2 e^{-i\Delta_K(t-t')} = |F_{-K_r}|^2 \sum_{K<0} e^{-i\Delta_K(t-t')} + |F_{+K_r}|^2 \sum_{K>0} e^{-i\Delta_K(t-t')}. \tag{S42}$$

Here, we separate the summation into $\pm K$, because the interference of the four decay channels results in $|F_{+K_r}| \neq |F_{-K_r}|$. We approximate the dispersion of the doublon state as linear around K_r, delineated by a group velocity v_{g}. Therefore, $\Delta_K = E_K - E_{K_r} = v_{\mathrm{g}}\delta K$, with $\delta K = K - K_r$. Under the Markovian approximation, we obtain

$$\begin{aligned}\sum_{K<0(K>0)} e^{-i\Delta_K(t-t')} = \sum_{K<0(K>0)} e^{-i(E_K-2\Delta_{\mathrm{e}})(t-t')} &= \pm\frac{N}{2\pi}\int_{\mp\pi}^{0} dK\ e^{-i(E_K-E_{\mp K_r})(t-t')} \\ &\simeq \frac{N}{2\pi v_{\mathrm{g}}}\int_{-\infty}^{\infty} e^{-iv_{\mathrm{g}}\delta K(t-t')}\ d(v_{\mathrm{g}}\delta K) = \frac{N}{v_{\mathrm{g}}}\delta(t-t').\end{aligned} \tag{S43}$$

Finally, the evolution equation for the GEP is

$$\begin{aligned}\dot{c}_{\mathrm{e}}(t) &= -\frac{g^4}{v_{\mathrm{g}}J^2}\left(|F_{-K_r}|^2 + |F_{K_r}|^2\right)\int_0^t dt'\ c_{\mathrm{e}}(t')\delta(t-t') \\ &= -\frac{g^4}{2v_{\mathrm{g}}J^2}\left(|F_{-K_r}|^2 + |F_{K_r}|^2\right)c_{\mathrm{e}}(t).\end{aligned} \tag{S44}$$

The supercorrelated decay is given by

$$c_{\mathrm{e}}(t) = e^{-\frac{\Gamma_+ + \Gamma_-}{2}t}, \quad \Gamma_\pm = \frac{g^4}{v_{\mathrm{g}}J^2}|F_{\pm K_r}|^2, \tag{S45}$$

where $\Gamma_\pm$ denote the emission rates into the right and left propagation directions. To characterize the unidirectional emission, we define the chiral factor as

$$C = \frac{\Gamma_+ - \Gamma_-}{\Gamma_+ + \Gamma_-} = \frac{|F_{+K_r}|^2 - |F_{-K_r}|^2}{|F_{+K_r}|^2 + |F_{-K_r}|^2}. \tag{S46}$$

In the above theoretical analysis, several standard approximations (adiabatically eliminating the intermediate states, the Born–Markov approximation, etc) were employed. To check the validity of the theoretical results in this study, we also perform numerical simulations by considering an open-boundary waveguide with length $N = 3000$ in real space. In the two-excitation subspace, the dimension of this Hilbert space is approximately $N_{\mathrm{H}} \simeq N^2/2 = 5\times 10^6$. In Fig. S3, we present a logical flow chart of how to obtain the numerical and analytical results in Fig. S2, and they agree well with each other throughout our work. Figure S2(b, c) displays the decay rate Γ and the chiral factor C as functions of the emitter frequency Δ_{e}, obtained by numerical simulations. In the same figure panels, we also plot the analytical results from Eq. (S45) and Eq. (S46), respectively. When Δ_{e} approaches $-2J$, the single-photon process will have apparent effects. Therefore, the supercorrelated decay rate predicted by Eq. (S45) cannot match well with the numerical simulations for those parameter values.

Under the conditions $\Phi_1^{\mathrm{e}} = \Phi_2^{\mathrm{e}} = \pi/2$ and $d = 1$, the chiral factor reaches its maximum $C = 1$ at $\Delta_{\mathrm{e}} = -2.55J$ ($K_r = 1.317$), coinciding with the zero point of $|F_{-K_r}|$ [dashed line in Fig. S2(c)], which we refer to as the "optimal point" for chiral emission. Once Δ_{e} is biased away from this point, the chiral factor decreases. Notably, the photon field mostly distributes around the line $r_{\mathrm{d}} = 0$, indicating that two photons in the emission field strongly bind together. To describe the spatial correlation properties of the photonic field, we define the two-point correlation function for the photonic field at $t \to \infty$:

$$\mathcal{G}^{(2)}(r_{\mathrm{d}}) = \sum_n \frac{\langle a^\dagger_{n+r_{\mathrm{d}}} a^\dagger_n a_{n+r_{\mathrm{d}}} a_n\rangle}{\langle a^\dagger_{n+r_{\mathrm{d}}} a_{n+r_{\mathrm{d}}}\rangle\langle a^\dagger_n a_n\rangle}. \tag{S47}$$

Figure 2(b) in the main text shows that, in the presence of the local nonlinear potential, the two-photon field exhibits the strongest correlation at $r_{\mathrm{d}} = 0$, which rapidly decreases with the two-photon separation distance r_{d}, i.e., $\mathcal{G}^{(2)}(r_{\mathrm{d}} \neq 0) \ll \mathcal{G}^{(2)}(0)$. Thus our proposal successfully generates directional emission of strongly correlated photon pairs (SCPPs).

C. Effects of the parameters of the GEP on decay and chiral

Equations (S45) and (S46) gives the analytical expressions of the decay rate and chiral factor, respectively. Leveraging these expressions, we now analyze how the geometric and coupling parameters of the GEP shape its dynamics.

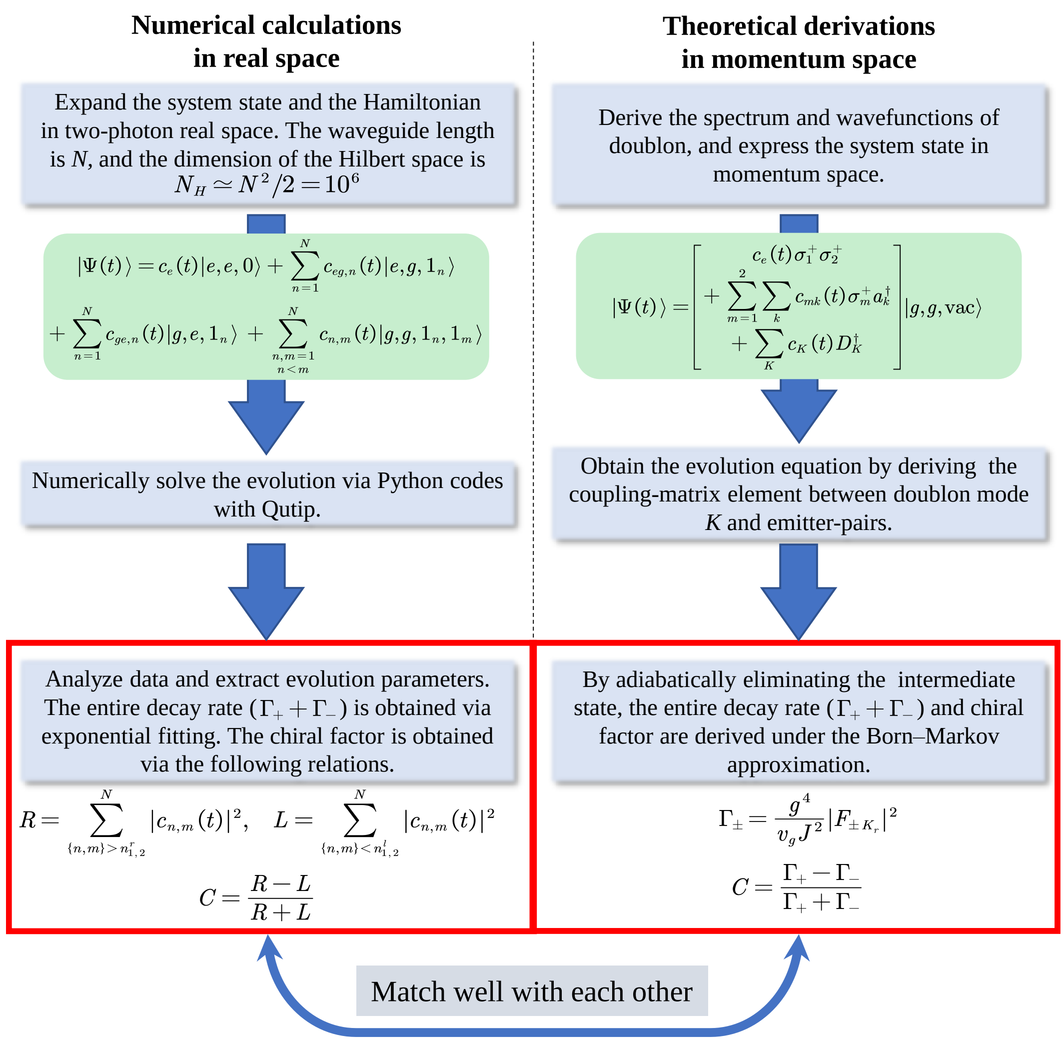

Figure S3. **The logical flow chart of numerical and analytical results.** The logical flow chart of how to obtain the numerical and analytical results in Fig. S2. The two results match well.

1. *Effects of the geometric layout of the GEP and coupling phases*

We now discuss how the size of a giant emitter, d, and the distance between the giant emitters, D, affect the interference among the decay channels. As indicated by Eq. (S40), we find that the distance between two points n_1^τ and n_2^g influences both the amplitude $A(r_{\rm d}^{\tau\sigma})$ and the propagation phase $\Phi_{\rm d}(x_{\rm c}^{\tau\sigma})$ of each channel (τ, σ). To demonstrate their effects we present, in Fig. S4, a bubble chart, showing the decay rate Γ and the chiral factor C as functions of D and d. The size (color) of the bubble represents the decay rate Γ (chiral factor C). Additionally, we depict three sections of the bubble chart along the lines $D = 0$, $D = d$, and $d = 6$, which are respectively plotted in Fig. S4(b)-(d). The red squares depict the decay rates obtained from numerical simulations, while the curves with circles represent the analytical solution using Eq. (S45). The bar graphs depict the amplitudea of the four vectors $A(r_{\rm d}^{\tau\sigma})$, which represent the contribution weights of the four decay channels. The chosen parameters are $K_r = \pi/2$ and $\Phi_1^{\rm e} = \Phi_2^{\rm e} = \pi/3$. We plot the corresponding GEP layout in the insets for each case. In Fig. S4(a), we first find that when increasing D (fixing d), the chiral factor changes little while the decay rate $\Gamma_\pm$ quickly decreases to zero. We also find that:

(i) $d = 1$ and $D = 0$. In this case, all the four decay channels will interfere with each other. Both the decay rate and the chiral factor are decided by the interference between these channels, as discussed in the main text.

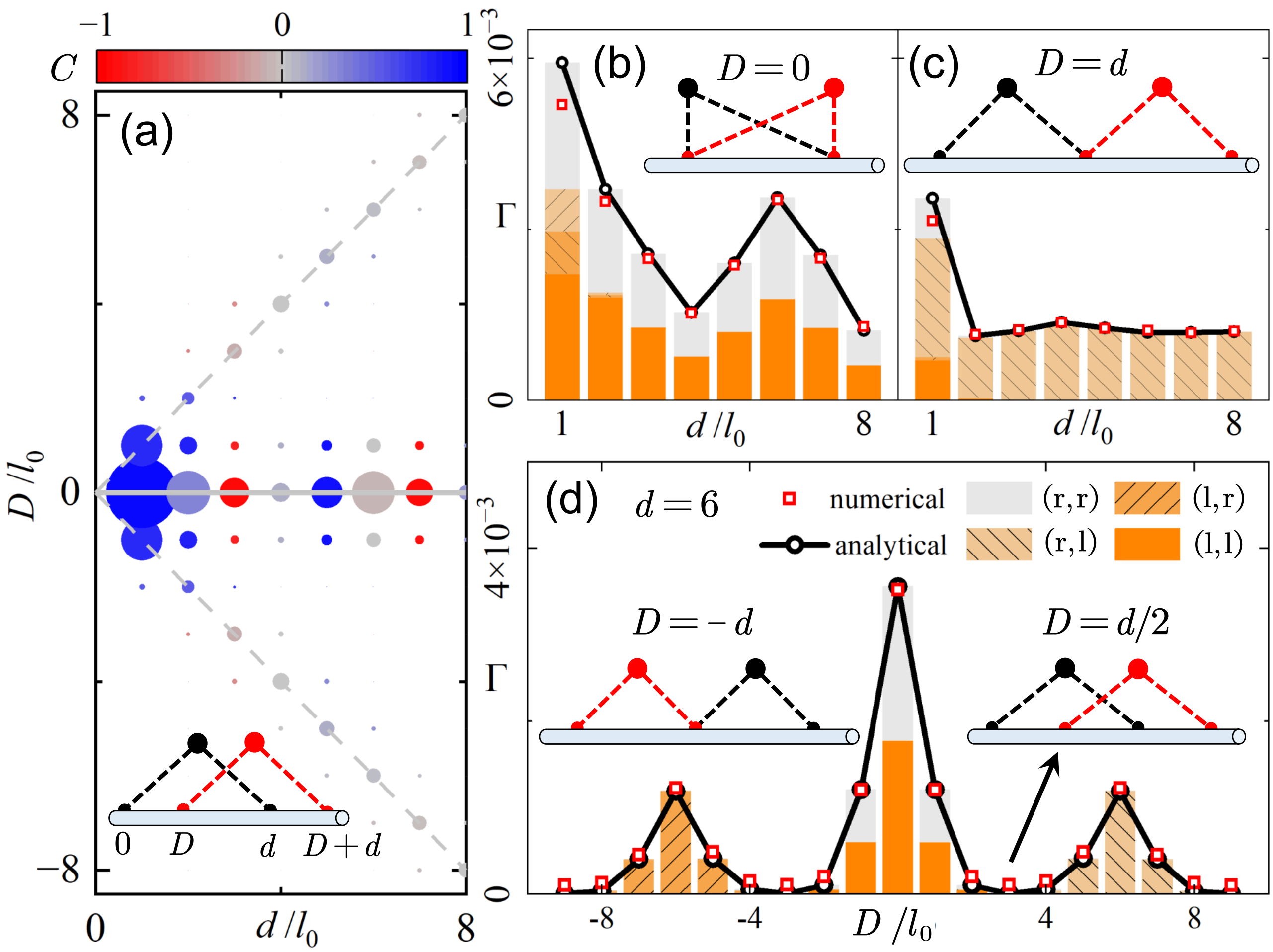

Figure S4. **Effects of the geometric layout of the GEP.** (a) The bubble chart illustrates the effects of the geometric layout of a giant-emitter pair on the decay rate and the chiral factor. The bubble size represents the decay rate, while the color shows the chiral factor. The gray solid line denotes the case $D = 0$. The gray dashed lines denote the cases $D = \pm d$. (b, c) The decay rate as a function of d by fixing $D = 0$ and $D = d$, respectively. (d) The decay rate as a function of D for $d = 6$. The different layouts are represented in the insets. Bar graphs inside (b–d) represent the contributions of the four decay channels. We fix $\Phi_1^{\mathrm{e}} = \Phi_2^{\mathrm{e}} = \pi/3$: the other parameters are the same as in Fig. 2 in the main text.

(ii) $d > L_u(K_r)$ and $D = 0$. As shown in Fig. S4(b),

$$A(r_{\mathrm{d}}^{\mathrm{ll}\,/\,\mathrm{rr}} = D = 0) \gg A(r_{\mathrm{d}}^{\mathrm{rl}\,/\,\mathrm{lr}}) \simeq 0, \tag{S48}$$

which indicates that only the two channels (l, l) and (r, r) contribute significantly to the interference, while the channels (r,l) and (l,r) have vanishingly small contributions. Therefore, the decay rate is approximately

$$\Gamma \propto \sum_{\pm} |F_{\pm K_r}|^2 \simeq 4A(0)[1 + \cos(\Phi_1^{\mathrm{e}} + \Phi_2^{\mathrm{e}}) \cos(K_r d)]. \tag{S49}$$

Since $\Phi_{1,2}^{\mathrm{e}}$ and K_r are fixed, Γ exhibits a cosine dependence on d, as shown in the large-d region of Fig. S4(b). Meanwhile, the chiral factor is simplified as

$$C = \frac{|F_{+K_r}|^2 - |F_{-K_r}|^2}{|F_{+K_r}|^2 + |F_{-K_r}|^2} \simeq \frac{\sin(\Phi_1^{\mathrm{e}} + \Phi_2^{\mathrm{e}}) \sin(K_r d)}{1 + \cos(\Phi_1^{\mathrm{e}} + \Phi_2^{\mathrm{e}}) \cos(K_r d)}. \tag{S50}$$

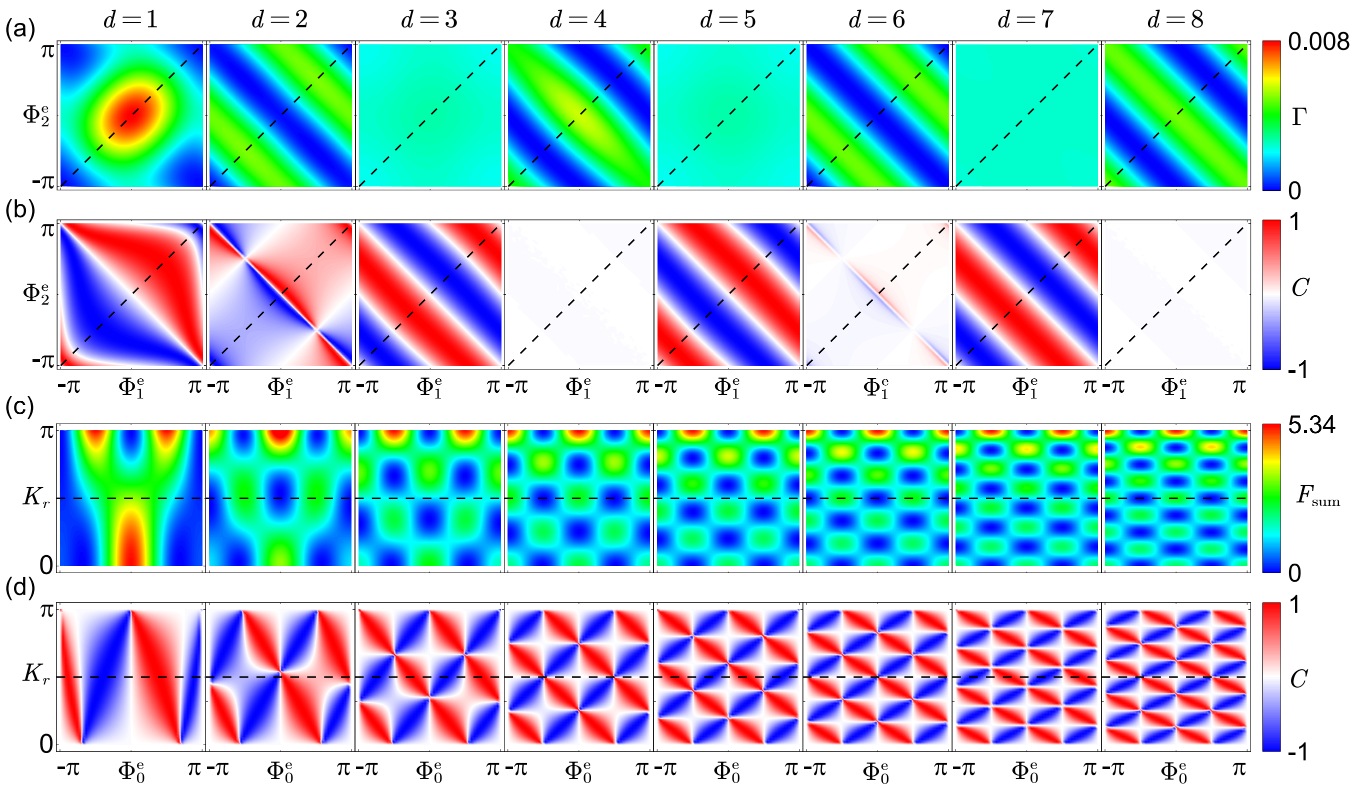

Figure S5. **The pattern for emitter dynamics parameters.** (a) Decay rate and (b) chiral factor, as functions of Φ_1^{e} and Φ_2^{e} for different giant-emitter sizes d, with $K_r = \pi/2$ ($\Delta_{\mathrm{e}} = -2.61J$) indicated by the black dashed line in (c, d). (c) $F_{\mathrm{sum}} = F(+K_r) + F(-K_r)$ and (d) chiral factor, as functions of K_r and $\Phi_0^{\mathrm{e}} = \Phi_1^{\mathrm{e}} = \Phi_2^{\mathrm{e}}$ [anti-diagonal black dashed line in (a, b)]. The other parameters are the same as in Fig. 2 of the main text.

In that scenario, C also exhibits a cosine dependence on d, as shown in the large-d region with $D = 0$ of Fig. S4(a).

(iii) $d > L_u(K_r)$ and $D > L_u(K_r)$. As shown in Fig. S4(c), under this condition, the channels (r, r) and (l, l) approximately vanish, with $A(r_{\mathrm{d}}^{\mathrm{rr}\,/\,\mathrm{ll}} = D) \simeq 0$. The SPCC can be emitted from a single channel (r, l), with $A(r_{\mathrm{d}}^{\mathrm{rl}} = |d - D|)$ and $d = D$, as depicted in the inset of Fig. S4. Therefore, the decay rate is

$$\Gamma \propto \sum_{\pm} |\vec{e}_{\mathrm{rl}}(\pm K)|^2 = A^2(r_{\mathrm{d}}^{\mathrm{rl}}), \tag{S51}$$

which shows that only one channel has significant effect, and the interference disappears, with no directional preference for the emitted field. This point can be verified from Fig. S4(a, c), where along the diagonal dashed grey lines $D = \pm d$, the chiral factor is $C = 0$.

2. *Effects of the coupling phases and resonance frequency*

We now focus on the case $D = 0$, and discuss how the coupling phases $\Phi_{1,2}^{\mathrm{e}}$ and the resonance mode K_r (linked to the emitter frequency via $2\Delta_{\mathrm{e}} = E_K$) shape GEP dynamics. In the main text, F_K is written as the sum of four vectors

$$F_K = \sum_{\tau,\sigma} \vec{e}_{\tau\sigma}(K), \tag{S52}$$

corresponding to the four decay channels in Fig. 3. Up to a global phase Φ_0, these vectors are:

$$\begin{aligned}
&\vec{e}_{\rm ll} : A_{\rm ll},\\
&\vec{e}_{\rm lr} : A_{\rm lr}\, e^{i\Phi_2^{\rm e}} e^{-iKd/2},\\
&\vec{e}_{\rm rl} : A_{\rm rl}\, e^{i\Phi_1^{\rm e}} e^{-iKd/2},\\
&\vec{e}_{\rm rr} : A_{\rm rr}\, e^{i\Phi_1^{\rm e}} e^{i\Phi_2^{\rm e}} e^{-iKd},
\end{aligned}$$

Owing to symmetry and $D = 0$, the amplitudes satisfy $A_{\rm ll} = A_{\rm rr} = A(0)$ and $A_{\rm lr} = A_{\rm rl} = A(d)$. Equation (S52) then simplified to

$$F(K) = A(0)\left[1 + e^{i\Phi_1^{\rm e}} e^{i\Phi_2^{\rm e}} e^{-iKd}\right] + A(d)\left[e^{i\Phi_2^{\rm e}} + e^{i\Phi_1^{\rm e}}\right] e^{-iKd/2}. \tag{S53}$$

From this expression, we derive

$$\begin{aligned}
&|F(+K)|^2 + |F(-K)|^2 =\\
&4A(0)^2\left[1 + \cos\left(\Phi_1^{\rm e} + \Phi_2^{\rm e}\right)\cos(2\theta)\right] + 8A(0)A(d)\cos(\theta)\left[\cos\left(\Phi_1^{\rm e}\right) + \cos\left(\Phi_2^{\rm e}\right)\right] + 4A(d)^2[1 + \cos\left(\Phi_1^{\rm e} - \Phi_2^{\rm e}\right)], \qquad \text{(S54)}\\
&|F(+K)|^2 - |F(-K)|^2 =\\
&8A(0)\sin(\theta)\left\{A(0)\sin(\Phi_1^{\rm e} + \Phi_2^{\rm e})\cos(\theta) + A(d)\left[\sin(\Phi_1^{\rm e}) + \sin(\Phi_2^{\rm e})\right]\right\}, \qquad \text{(S55)}
\end{aligned}$$

where $\theta = Kd/2$.

In Fig. S5(a, b), we plot the decay rate Γ and chiral factor C as functions of $\Phi_1^{\rm e}$ and $\Phi_2^{\rm e}$ for different d, with $K = K_r = \pi/2$ [indicated by black dashed lines in Fig. S5(c, d)]. To isolate interference effects from dispersion-induced group velocity $v_{\rm g}$ [the denominator of the decay rate in Eq. S45], we analyze the sum amplitude $F_{\rm sum} = |F(+K)|^2 + |F(-K)|^2$ and C in the $(K, \Phi_0^{\rm e})$ plane, setting $\Phi_0^{\rm e} = \Phi_1^{\rm e} = \Phi_2^{\rm e}$ [anti-diagonal in Fig. S5(a, b)]. Via the dispersion relation $2\Delta_{\rm e} = E_K = -\sqrt{U^2 + 16J^2\cos^2(K/2)}$, the wavevector K directly maps to the emitter frequency.

We identify two distinct regimes:

1. Short separation ($d = 1$). All four channels contribute significantly. Both Γ and C reflect the interference among the four vectors.

2. Long separation [$d > L_u(K_r)$], where $A(d) \simeq 0$. The expressions Eqs. (S54) and (S55) reduce to

$$|F(+K)|^2 + |F(-K)|^2 \approx 4A^2(0)[1 + \cos(\Phi_+^{\rm e})\cos(Kd)], \tag{S56}$$

$$|F(+K)|^2 - |F(-K)|^2 \approx 4A^2(0)\sin(\Phi_+^{\rm e})\sin(Kd), \tag{S57}$$

with the symmetric phase $\Phi_+^{\rm e} = \Phi_1^{\rm e} + \Phi_2^{\rm e}$.

In Fig. S5(a, b) ($K = \pi/2$), Γ and C exhibit pronounced interference patterns:

- For Γ (panel a): When $\cos(Kd) = 0$ ($d = 3, 5, 7$), Γ becomes uniform. At $d = 4,\ 8$ [$\cos(Kd) = 1$], diagonal striped pattern appear, with alternating bright (green) and dark (blue) bands modulated by $\cos(\Phi_+^{\rm e})$; while the pattern inverts for $d = 6$ [$\cos(Kd) = -1$].
- For C (panel b): When $\sin(Kd) = 0$ ($d = 4,\ 6,\ 8$), C vanishes. At $d = 3,\ 7$ [$\sin(Kd) = -1$], a similar striped pattern appears, with red (positive) and blue (negative) bands separated by nodal lines at $\sin(\Phi_+^{\rm e}) = 0$ ($\Phi_+^{\rm e} = 0, \pm\pi$); the contrast flips for $d = 5$ [$\sin(Kd) = 1$].

In Fig. S5(c, d), the full $(K, \Phi_0^{\rm e})$ dependence is shown:

- $F_{\rm sum}$ (panel c) displays a checkerboard-like pattern. Horizontal variations (in $\Phi_0^{\rm e}$) follow a cosine envelope, while vertical oscillations (in K) become denser with increasing d. The overall intensity grows with K due to the K-dependence of $A(0)$.
- C (panel d) forms a diamond lattice of alternating red/blue domains, reflecting sine dependence on $\Phi_0^{\rm e}$ and Kd. Similarly, as d increases, vertical oscillation (in K) become denser. Nodal lines (white) are given by $\sin(Kd) = 0$ or $\sin(\Phi_0^{\rm e}) = 0$.

Moreover, the red (blue) regions in Fig. S5(b, d), corresponding to $C = +1$ ($C = -1$), identify optimal parameters for unidirectional emission: the optimal mode K (i.e., emitter frequency $\Delta_{\rm e}$) together with coupling phases $\Phi_1^{\rm e}$ and $\Phi_2^{\rm e}$.

These complex interference results demonstrate that both the super-correlated decay rate Γ and chirality C can be engineered via the geometric parameters d and D, as well as the encoded phases $\Phi_{1,2}^{\rm e}$, and resonance frequency $2\Delta_{\rm e}$.

3. Nodal conditions for the chiral factor

The chiral factor C vanishes when the right and left emission intensities balance, i.e., $|F(+K)|^2 - |F(-K)|^2 = 0$. In that scenario, the GEP dynamics recover the small atom behaviour, with non-directional emission [S2]. From Eq. (S55), this occurs when

$$\sin(\theta)\sin\left(\frac{\Phi_1^{\mathrm{e}}+\Phi_2^{\mathrm{e}}}{2}\right)\left[A(0)\cos\theta\cdot\cos\left(\frac{\Phi_1^{\mathrm{e}}+\Phi_2^{\mathrm{e}}}{2}\right)+A(d)\cos\left(\frac{\Phi_1^{\mathrm{e}}-\Phi_2^{\mathrm{e}}}{2}\right)\right]=0. \tag{S58}$$

This condition is satisfied in three distinct scenarios:

$$\theta=\frac{Kd}{2}=m\pi,\quad m\in\mathbb{Z}, \tag{S59a}$$

$$\Phi_1^{\mathrm{e}}+\Phi_2^{\mathrm{e}}=2m\pi,\quad m\in\mathbb{Z}, \tag{S59b}$$

$$A(0)\cos\theta\cdot\cos\left(\frac{\Phi_1^{\mathrm{e}}+\Phi_2^{\mathrm{e}}}{2}\right)+A(d)\cos\left(\frac{\Phi_1^{\mathrm{e}}-\Phi_2^{\mathrm{e}}}{2}\right)=0. \tag{S59c}$$

- Equation Eq. (S59a), implies that for suitable separations and resonance modes $Kd = 2m\pi$, the system cannot support directional emission regardless of coupling phases, as shown in Fig. S5(b) for $d = 4,\ 6,\ 8$ and the horizontal white bands in Fig. S5(d).
- Equation Eq. (S59b), defines a diagonal line in the phase plane, independent of K or d, visible as a white diagonal in Fig. S5(b) and vertical white zones at $2\Phi_0^{\mathrm{e}} = \Phi_1^{\mathrm{e}} + \Phi_2^{\mathrm{e}} = 0, 2\pi$ in Fig. S5(d).
- Equation Eq. (S59c), yields curved nodal lines depending on both K, d (via θ) and $A(d)$, accounting for the remaining white features in Fig. S5(b,d).

D. Results for repulsive interaction $U > 0$

We now turn to the case of repulsive interaction $U > 0$. By replacing the dispersion relation and the wavefunction in Eqs. (15) and (17) with those in Eqs. (16) and (18) throughout the derivation, we obtain the numerical and analytical results for $U > 0$. Figure. S6 displays the decay rate Γ and the chiral factor C as functions of the phase $\Phi_{1,2}^{\mathrm{e}}$ over an extended range of $[-2\pi, 2\pi]$, comparing repulsive ($U > 0$) and attractive ($U < 0$) interactions. Under a π-phase shift, the decay rate remains invariant, while the chirality is reversed due to the energy relation $E_K^{(U>0)} = -E_K^{(U<0)}$. To illustrate these dynamics, we present the time evolution and the photonic field distribution for two cases: (i) $U < 0$, $\Delta_{\mathrm{e}} < 0$, $\Phi_{1,2}^{\mathrm{e}} = -\pi/5$ and (ii) $U > 0$, $\Delta_{\mathrm{e}} > 0$, $\Phi_{1,2}^{\mathrm{e}} = -\pi/5 + \pi = 4\pi/5$. These distinctive properties stem from the sign alternation of the wavefunction between nearest-neighbor r under repulsive ($U > 0$), combined with the reversal of the dispersion relation, as shown in Fig. S1.

E. Effects of frequency mismatch of a single emitter

In the previous discussion, we assumed that the two emitters in one pair were identical with the same frequency, i.e., $\omega_{\mathrm{e}1} = \omega_{\mathrm{e}2} = \omega_{\mathrm{e}}$. Now we explore how a slight shift in the frequencies of the individual emitters influences the dynamics. As shown in Fig. S7(a), we introduce a detuning in the frequency of each emitter, while keeping the sum of the frequencies constant, i.e.,

$$\begin{gathered}\omega_{\mathrm{e}1}=\omega_{\mathrm{e}}-\delta\omega,\quad \omega_{\mathrm{e}2}=\omega_{\mathrm{e}}+\delta\omega,\\ \omega_{\mathrm{e}1}+\omega_{\mathrm{e}2}=2\omega_{\mathrm{e}}.\end{gathered} \tag{S60}$$

In the frame rotating with w_{c}, when $\Delta_{\mathrm{e}2} = \omega_{\mathrm{e}2} - \omega_c < -2J$, the single emitter remains below the single-photon scattering band, and the frequency sum still lies in the doublon state. Therefore, the GEP continues to emit a super-correlated photon pair, but with a slightly different effective coupling strength. The evolution equation is modified as

$$i\dot{c}_{mk}(t)=\delta_{ki}c_{mk}(t)+\sum_{\tau=\mathrm{l,r}}\left[\frac{g}{\sqrt{N}}e^{-ikn_{m'}^{\tau}}e^{i\phi_{m'}^{\tau}}c_{\mathrm{e}}(t)+ge^{-i\phi_m^{\tau}}M(k,n_m^{\tau},K)c_K(t)\right]. \tag{S61}$$

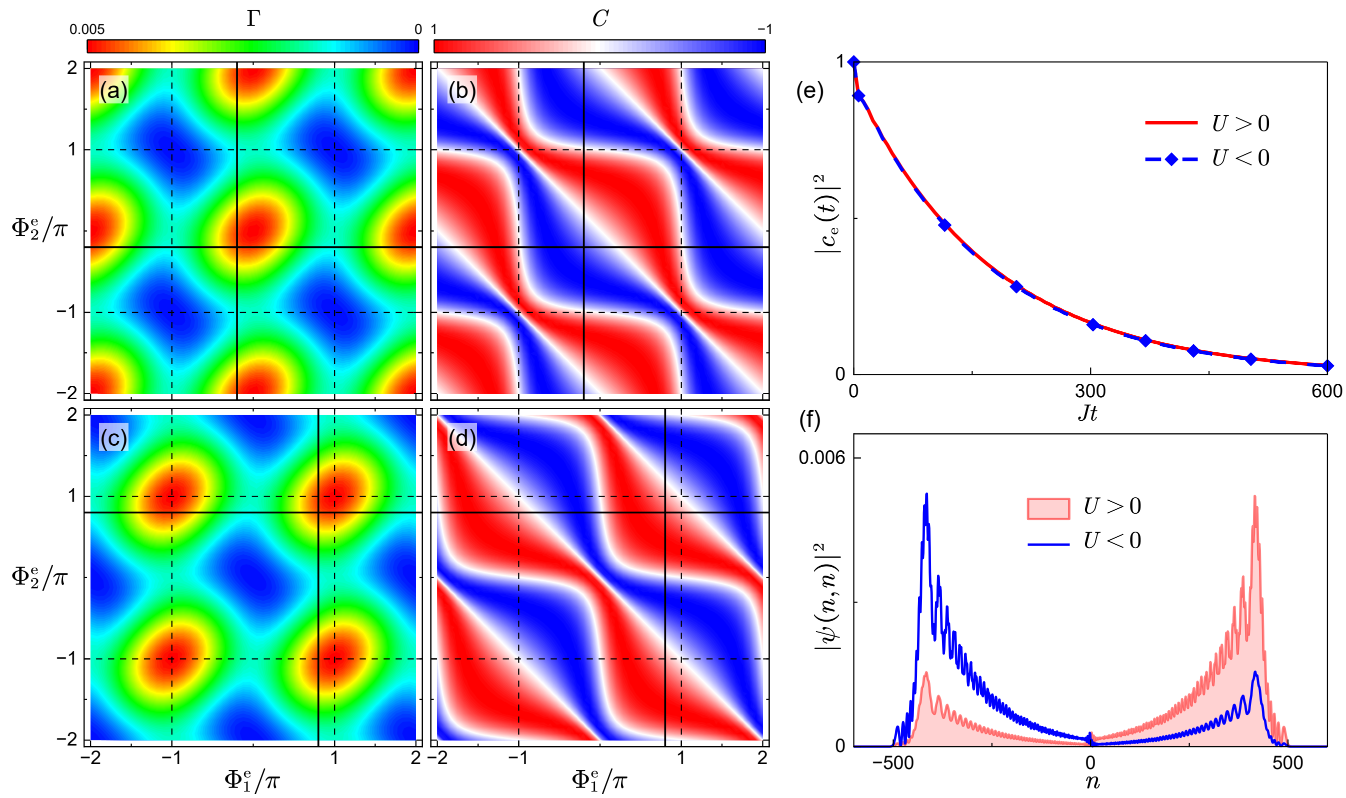

Figure S6. **The chirality for different nonlinearity.** (a) Decay rate Γ and (b) chiral factor C as functions of $\Phi_1^(e)$ and $\Phi_2^(e)$ over $[-2\pi, 2\pi]$ for the attractive interaction $U<0$. (c, d) Corresponding plots of Γ and C for the repulsive interaction $U>0$. Dashed lines mark the first Brillouin zone boundaries. Solid lines indicate the parameter sets $\Phi_1^{\rm e}, \Phi_2^{\rm e} = -\pi/5$ (for $U<0$) and $4\pi/5$ (for $U>0$) used in (e) and (f). (e) Time evolution of $|c_{\rm e}(t)|^2$. (f) Photonic field distribution $|\psi(n,n)|$ at $Jt=600$. In (e) and (f), red curves correspond to $U>0$, $\Delta_{\rm e}>0$, and $\Phi_{1,2}^{\rm e}=4\pi/5$; blue curves correspond to $U<0$, $\Delta_{\rm e}<0$, and $\Phi_{1,2}^{\rm e}=-\pi/5$. Parameters: $d=1$, $g=0.1J$, $|U|=4J$, $2|\Delta_{\rm e}|=5.1J$.

Here, $\delta_{ki}=\omega_k-\Delta_{\rm e}-(-1)^i\delta\omega=\delta_k-(-1)^i\delta\omega$. The F_K [Eq. (S32)] derived as

$$F_K=\sum_{m=1}^{2}\sum_k \frac{J}{\delta_k}\left[\frac{1}{1-\left(\frac{\delta\omega}{\delta_k}\right)^2}+(-1)^m\frac{\delta_k\delta\omega}{\delta_k^2-(\delta\omega)^2}\right]\left[\sum_{\tau=\mathrm{l,r}} e^{i\phi_m^\tau}e^{-ikn_m^\tau}\right]\left[\sum_{\sigma=\mathrm{l,r}} e^{i\phi_{m'}^\tau}M^*(k,n_{m'}^\tau,K)\right]. \tag{S62}$$

Substituting the expression of $M(k,n,K)$ into F_K, we rewrite F_K as

$$\begin{aligned}F_K=&\sum_{\tau,\sigma=\mathrm{l,r}}\sum_k\frac{1}{1-\left(\frac{\delta\omega}{\delta_k}\right)^2}\cos[(k-K/2)(n_1^\tau-n_2^\sigma)]e^{i\phi_1^\tau}e^{i\phi_2^\sigma}e^{-i(n_1^\tau+n_2^\sigma)K/2}L_{k,K}\\&-\sum_{\tau,\sigma=\mathrm{l,r}}\sum_k\frac{\delta_k\delta\omega}{\delta_k^2-(\delta\omega)^2}\sin[(k-K/2)(n_1^\tau-n_2^\sigma)]e^{i\phi_1^\tau}e^{i\phi_2^\sigma}e^{-i(n_1^\tau+n_2^\sigma)K/2}L_{k,K}.\end{aligned} \tag{S63}$$

In the scenario where $D=0$, $d\neq0$ [$n_1^{l(r)}-n_2^{l(r)}=0$, $n_1^{\rm r}-n_2^{\rm l}=-(n_1^{\rm l}-n_2^{\rm r})$], and $\Phi_1^{\rm e}=\Phi_2^{\rm e}$, the sine part of F_K becomes zero. Equation (S63) is then simplified to

$$F_K=\sum_{\tau,\sigma=\mathrm{l,r}}\sum_k\frac{1}{1-\left(\frac{\delta\omega}{\delta_k}\right)^2}\cos[(k-K/2)(n_1^\tau-n_2^\sigma)]e^{i\phi_1^\tau}e^{i\phi_2^\sigma}e^{-i(n_1^\tau+n_2^\sigma)K/2}L_{k,K}, \tag{S64}$$

which differs from F_K in Eq. (S36) only by a small coefficient $[1-(\delta\omega/\delta_k)^2]^{-1}$.

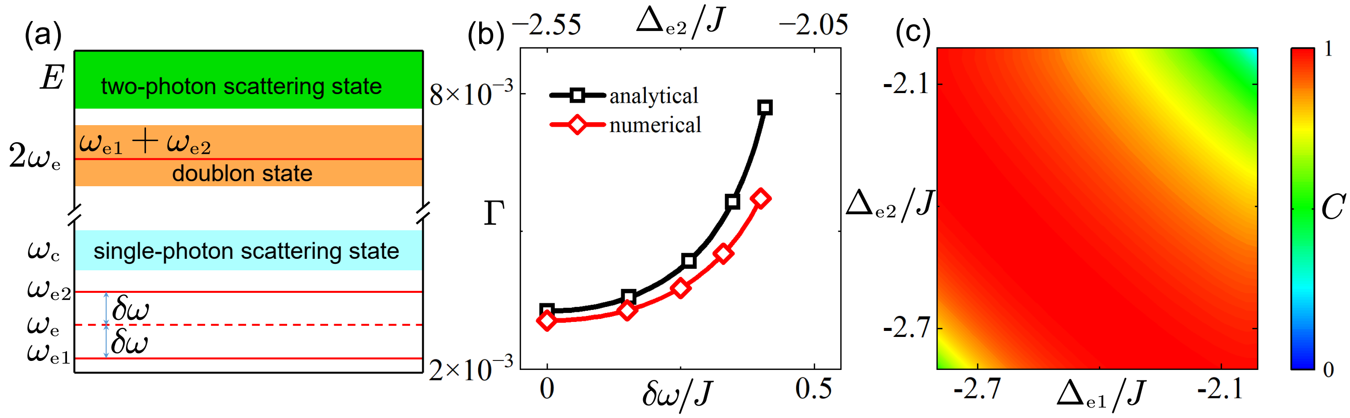

Figure S7. **Effects of frequency mismatch.** (a) The relations between the energy levels of the two emitters with frequencies ω_{e1} and ω_{e2} and the waveguide spectrum. The red lines denote the frequency of the emitters. (b) The decay rate as a function of the frequency mismatch $\delta\omega$. The analytical results (black squares) are plotted using Eq. (S64). (c) The chiral factor C as a function of the frequency of the two emitters $\Delta_{e1,\,e2} = \omega_{e1,\,e2} - \omega_c$. The parameters are the same as in Fig. 2 in the main text.

In Fig. S7(b), we plot the decay rate as a function of $\delta\omega$ via numerical simulations with a finite waveguide, which match well with the analytical results predicted by Eq. (S64). We find that the decay rate increases with the frequency mismatch $\delta\omega$. When $\delta\omega$ becomes sufficiently large, resulting in ω_{e1} or ω_{e2} lying within the single-photon scattering state, single-photon emission occurs, leading to the disappearance of super-correlated emission. Figure S7(c) illustrates the chiral factor as a function of the single-emitter frequencies ω_{e1} and ω_{e2}. We find that the chiral factor does not change much with the frequency mismatch of a single emitter. The reason can be understood as being the following: the amplitude $|A_{\tau\sigma}|$ of each vector is slightly shifted by the frequency mismatch, but the encoded phase and the propagation phase remain the same. Therefore, the imprecision of the frequency of the emitter pair has little effect on the chiral factor.

F. Cascaded master equation for two giant-emitter pairs

In the main text, we obtain the nonlinear cascaded master equation. In this section, we demonstrate a numerical example. By setting the frequency of the four emitters to be identical and the GEP A initially in its excited state, in Fig. S8(a), we plot the time evolution of the two emitter pairs via numerical simulations with a finite waveguide ($N = 3000$), which matches well with the results from the master equation. The correlated photons emitted by GEP A are absorbed by GEP B without back-scattering. Therefore, GEP A will not be re-excited when $t \to \infty$.

Supplementary Note 3. APPLICATIONS WITH DIRECTIONALLY CORRELATED PHOTON PAIRS

Many applications in linear cascaded quantum networks, where quantum information is carried by single photons [S4–S6], can find their nonlinear counterparts with GEPs emitting and absorbing doublons. Moreover, comparing with a single flying qubit, more quantum information can be encoded into “correlated flying qubits”, enabling distinct applications beyond linear unidirectional setups. Our proposal is feasible in circuit-QED systems [S7–S9], where giant emitters have been implemented in experiments [S10–S12]. An array of coupled transmon qubits [S13–S17] can be configured as the nonlinear waveguide. In Table S1, we list representative experimental parameters. The nearest-neighbour hopping rate J and transmon nonlinearity U (referred to as “qubit anharmonicity”) are on the order of $J/(2\pi) \sim 50\,\mathrm{MHz}$ and $U/(2\pi) \sim 200\,\mathrm{MHz}$. As indicated in Fig. S7(b), the supercorrelated decay rate can therefore be estimated to be $\Gamma_\pm/(2\pi) \sim 1\,\mathrm{MHz}$. The intrinsic decay rate γ and dephasing rate κ of an individual transmon are usually (in a conservative estimate) around $\gamma/2\pi \simeq 5\,\mathrm{kHz}$ ($T_1 \sim 30\,\mu\mathrm{s}$) and $\kappa/2\pi \sim 3\,\mathrm{kHz}$ - $150\,\mathrm{kHz}$ ($T_2 \sim 1\,\mu\mathrm{s}$ - $50\,\mu\mathrm{s}$) [S18, S19]. We find that $\Gamma_\pm \gg \{\gamma, \kappa\}$, indicating that the predicted phenomena are possible to observe in current circuit-QED setups.

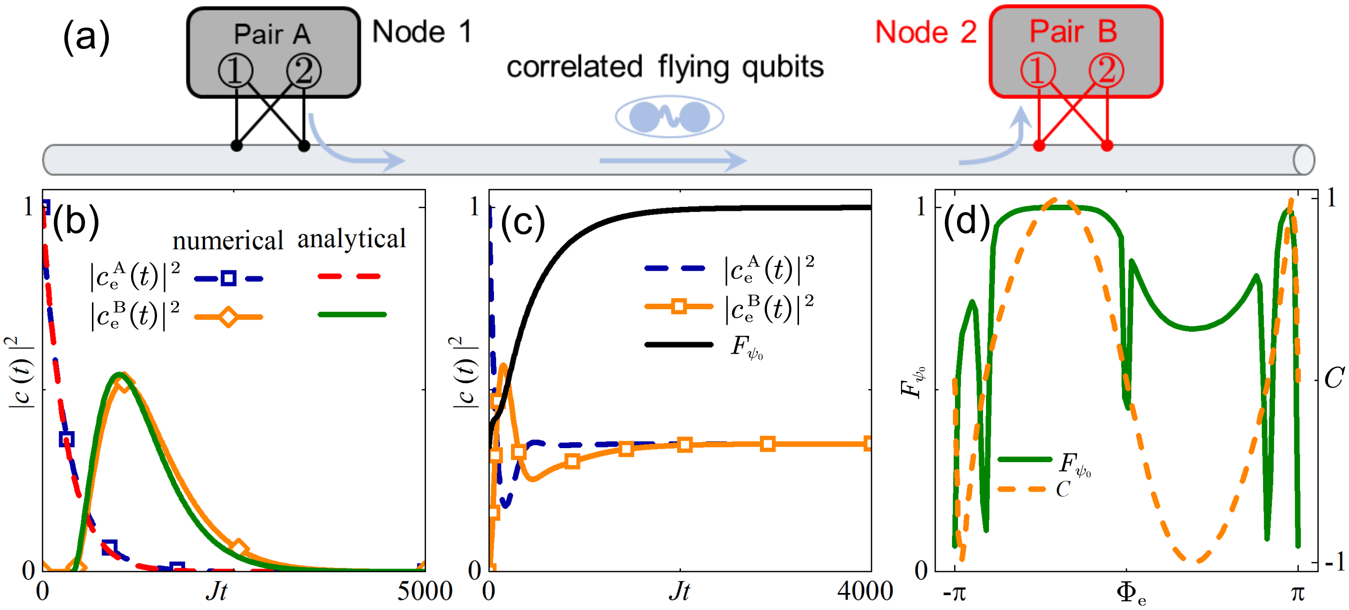

Figure S8. **Cascaded system for two giant-emitter pairs.** (a) The cascaded quantum system with two nodes connected by correlated photon pairs. (b) Time evolutions of the occupation probabilities in the cascaded system, obtained via numerical simulations with a finite waveguide and through simulation of the analytically derived master equation. The probabilities of the two emitters in pair A/B simultaneously being excited are denoted $|c_e^{A/B}(t)|^2$. At $t = 0$, we assume that GEP A (B) is in its excited (ground) states. (c) Time evolution of the fidelity F for the four-body entangled states (black solid curve), $|c_e^A(t)|^2$ (blue dashed curve), and $|c_e^B(t)|^2$ (orange solid curve with squares) in the presence of the coherent drive Ω_d. (d) Fidelity F_{ψ_0} (green curve) and chiral factor (orange dashed curve) as a function of $\Phi_e = \Phi^e_{1(2)}$. Same parameters as in Fig. 2 in the main text.

Reference	$J/(2\pi)$	$U/(2\pi)$	U/J
S. Hacohen-Gourgy *et al.* (2015) [S14]	~ 177 MHz	~ 240 MHz	1.4
P. Roushan *et al.* (2017) [S15]	~ 50 MHz	~ 175 MHz	3.5
G. P. Fedorov *et al.* (2021) [S16]	~ 41 MHz	~ 188 MHz	4.6
E. Kim *et al.* (2021) [S17]	~ 350 MHz	~ 297 MHz	0.85

Table S1. Experimental parameters for a representative sampling of published experiments with array of coupled transmons.

A. Steady four-partite entangled states between remote GEPs

Based on the above cascaded quantum systems mediated by "correlated flying qubits", we show how to generate steady four-partite entangled states between two remote nodes by applying additional parametric coherent drives to the two GEPs. As depicted in Fig. S9, we take circuit QED as an example.

Giant emitters 1 and 2 are coupled together via a Josephson loop, which is composed of two shared branches with inductances $L_{B1(2)}$ and a Josephson junction with an inductance L_C. To realize a parametric drive on the two emitters, we assume that a time-dependent flux through the loop is applied. As discussed in Refs. [S20, S21], the

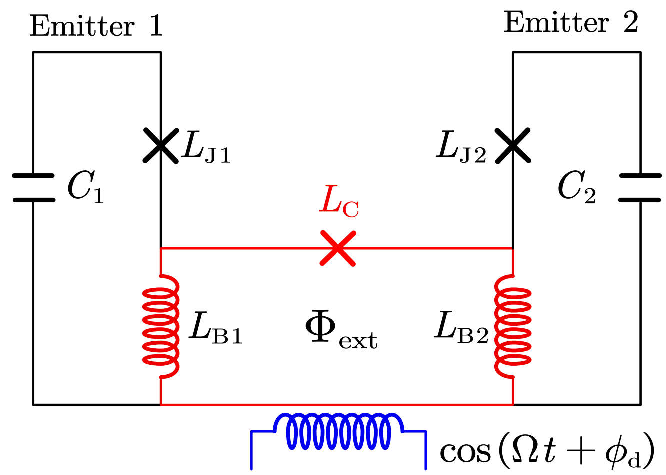

Figure S9. **Schematic realization of parametric driving for two emitters.** We take circuit QED as an example, with two transmons in the form of Josephson junctions (with effective inductances $L_{\mathrm{J}1,2}$) shunted by their capacitances $C_{1,2}$. The parametric coupling loop is composed of two shared inductances $L_{\mathrm{B}1,2}$ and a coupling Josephson inductance L_{C}. To induce a time-dependent interaction, an external flux $\phi_{\mathrm{ext}}(t)$ is applied through the loop.

Hamiltonian of the whole system is

$$H_{\mathrm{d}} = \sum_{i=1}^{2} \omega_{ei}\sigma_i^z + g(t)\big(\sigma_1^+ + \sigma_1^-\big)\big(\sigma_2^+ + \sigma_2^-\big), \tag{S65}$$

where the effective coupling between two emitters is controlled via the external flux produced by the current in the coil. For simplicity, we assume that the circuit parameters of the two emitters are identical, i.e., $L_{\mathrm{B}1(2)} = L_{\mathrm{B}}$, $L_{\mathrm{J}1(2)} = L_{\mathrm{J}}$, and $\omega_{\mathrm{e1,\,e2}} = \omega$. In the limit $L_{\mathrm{B}} \ll L_{\mathrm{C}}$, the relation between the coupling strength and the external flux is [S20]

$$g(t) \simeq \frac{L_{\mathrm{B}}^2\omega_q}{2(L_{\mathrm{J}} + L_{\mathrm{B}})L_{\mathrm{C}}}\cos[\phi_{\mathrm{ext}}(t)], \qquad \phi_{\mathrm{ext}}(t) = 2\pi\frac{\Phi_{\mathrm{ext}}(t)}{\Phi_0}. \tag{S66}$$

We assume that $\phi_{\mathrm{ext}}(t)$ is composed of a dc and an ac part, i.e., $\phi_{\mathrm{ext}}(t) = \pi/2 + A_{\mathrm{ext}}\cos(\Omega t + \phi_{\mathrm{d}})$. In the limit $A_{\mathrm{ext}} \ll \pi$, $g(t)$ is approximately given by

$$g(t) \simeq \Omega_{\mathrm{d}}\sin(\Omega t + \phi_{\mathrm{d}}), \qquad \Omega_{\mathrm{d}} = -\frac{L_{\mathrm{B}}^2\omega_q A_{\mathrm{ext}}}{2(L_{\mathrm{J}} + L_{\mathrm{B}})L_{\mathrm{C}}}. \tag{S67}$$

Given that $\Omega = \omega_{\mathrm{e1}} + \omega_{\mathrm{e2}}$, only the counter-rotating terms in Eq. (S65) are resonant and should be kept. The Jaynes–Cummings terms $\sigma_1^+\sigma_2^- + \mathrm{H.c.}$ are rapidly oscillating and can be neglected. In the rotating frame of emitter frequencies, H_{d} is reduced to a parametric-driving form, i.e.,

$$H_{\mathrm{d}} = \frac{\Omega_{\mathrm{d}}}{2}\sigma_1^+\sigma_2^+ + \mathrm{H.c.} \tag{S68}$$

where we set $\phi_{\mathrm{d}} = \pi/2$. When the parametric drives are applied to both GEP A and B, the effective Hamiltonian in Eq. (**??**) becomes

$$H'_{\mathrm{eff}} = H_{\mathrm{eff}} + \frac{\Omega_{\mathrm{d}}}{2}\big(S_{\mathrm{A}}^+ + S_{\mathrm{B}}^+ + \mathrm{H.c.}\big). \tag{S69}$$

We assume that the chiral factor is $C \simeq 1$ and that the two GEPs exclusively emit correlated photons into the right direction. Similar to the linear unidirectional quantum setups, the interplay between driving and directional dissipation leads to a dark state for the two GEPs [S6]:

$$\dot{\rho}_0 = -i[H_{\mathrm{eff}}, |\psi_0\rangle\langle\psi_0|] + \mathcal{L}|\psi_0\rangle\langle\psi_0|\mathcal{L}^\dagger = 0, \tag{S70}$$

By solving the above equation, we find that the two GEPs will be trapped in a four-body entangled steady state

$$|\psi_0\rangle = |gggg\rangle + i\frac{\sqrt{2}\Omega_{\rm d}}{\Gamma_+}|S\rangle, \qquad |S\rangle = \frac{|ggee\rangle - |eegg\rangle}{2}. \tag{S71}$$

Moreover, in the limit $\Omega_{\rm d} \gg \Gamma_+$, the dark state is approximately a four-body maximally entangled state

$$|\psi_0\rangle \simeq \frac{|ggee\rangle - |eegg\rangle}{\sqrt{2}}. \tag{S72}$$

By defining the fidelity $F_{\psi_0} = \langle\psi_0|\rho(t)|\psi_0\rangle$, we plot the time evolutions of the four emitters governed by $H'_{\rm eff}$ in Fig. S8(c), which shows that the two GEPs will be deterministically trapped in the state $|\psi_0\rangle$ in the steady state at long times. By setting $\Phi^{\rm e}_{1(2)} = \Phi_{\rm e}$, we plot the fidelity and chiral factor as functions of $\Phi_{\rm e}$ in Fig. S8(d). In the regions of right emission with $C \simeq 1$, the fidelity can reach 1. When $\Phi^{\rm e}_{1(2)}$ is biased away from the regime of the directional emission, the whole setup becomes bidirectional, and the fidelity for entangled states decreases accordingly, as shown in Fig. S8(d).

B. State transfer via modulating the coupling strength

By modulating the decay rate with time, the shape of the directional wave packet can be tailored freely. Under this mechanism, a perfect single-qubit state transfer process via a photonic wave packet with time-reversal symmetry, has been extensively explored in linear unidirectional setups [S6, S22–S24]. In this proposed nonlinear cascaded system, more quantum information can be encoded into "correlated flying qubits", and we show that a high-fidelity entangled-state transfer between GEP A and B can be realized.

At time t, the state of the cascaded system can be expanded as

$$|\psi(t)\rangle = c^{\rm A}_{\rm e}(t)e^{-i\Phi_-(t)}|eegg0_{\rm ch}\rangle + c^{\rm B}_{\rm e}(t)e^{i\Phi_-(t)}|ggee0_{\rm ch}\rangle + c_{\rm g}(t)e^{i\Phi_+(t)}|gggg0_{\rm ch}\rangle + \sum_K \alpha_K(t)\mathcal{D}^\dagger_K|gggg0_{\rm ch}\rangle, \tag{S73}$$

where $|eegg\rangle$ ($|ggee\rangle$) represents the two emitters of pair A (B) both being excited, and $|0_{\rm ch}\rangle$ denotes the waveguide in its vacuum state. The dynamical phase factors are [S25]

$$\Phi_\pm(t) = \frac{1}{2}\int_{t_0}^{t} dt' \ [\omega_{\rm A}(t') \pm \omega_{\rm B}(t')], \tag{S74}$$

where $\omega_{\rm A(B)}(t) = 2\omega_{\rm e} + \sum_{i=1,2}\delta\omega_{{\rm A(B)},i}(t)$ is the renormalized frequency of GEP A (B). Note that the Stark shift of each emitter due to the single-photon scattering state should be considered during state-transfer processes; it is given by

$$\delta\omega_{{\rm A(B)},i}(t) = -\frac{1}{N}\sum_k \frac{\left|g_{{\rm A(B)},i}(t)\right|^2}{\omega_{\rm c} + \omega_k - \omega_{\rm e}}, \tag{S75}$$

$$g_{{\rm A(B)},i}(t) = g_{\rm A(B)}(t)\sum_{\tau={\rm l,r}} e^{ikn^\tau_i} e^{i\phi^\tau_i} \tag{S76}$$

with $g_{{\rm A(B)},i}(t)$ the effective coupling strength. Note further that when $g_{\rm A(B)}(t)$ is modulated in time, the Stark shift for each GEP will also be time-dependent.

To realize a high-fidelity entangled-state transfer, we require that the whole system satisfies the dark-state condition

$$[S_{\rm A}(t) + S_{\rm B}(t)]|\psi(t)\rangle = 0, \tag{S77}$$

which restricts $\sqrt{\Gamma_{\rm A}(t)}c^{\rm A}_t(t) + \sqrt{\Gamma_{\rm B}(t)}c^{\rm B}_{\rm e}(t) = 0$ and $\alpha_K(t) = 0$ [S6]. Then, the evolution equations are $\dot{c}_{\rm g} = 0$ and

$$\dot{c}^{\rm A}_{\rm e}(t) = -\frac{\Gamma_{\rm A}(t)}{2}c^{\rm A}_{\rm e}(t), \tag{S78}$$

$$\dot{c}^{\rm B}_{\rm e}(t) = -\frac{\Gamma_{\rm B}(t)}{2}c^{\rm B}_{\rm e}(t) - \sqrt{\Gamma_{\rm A}(t)\Gamma_{\rm B}(t)}c^{\rm A}_{\rm e}(t). \tag{S79}$$

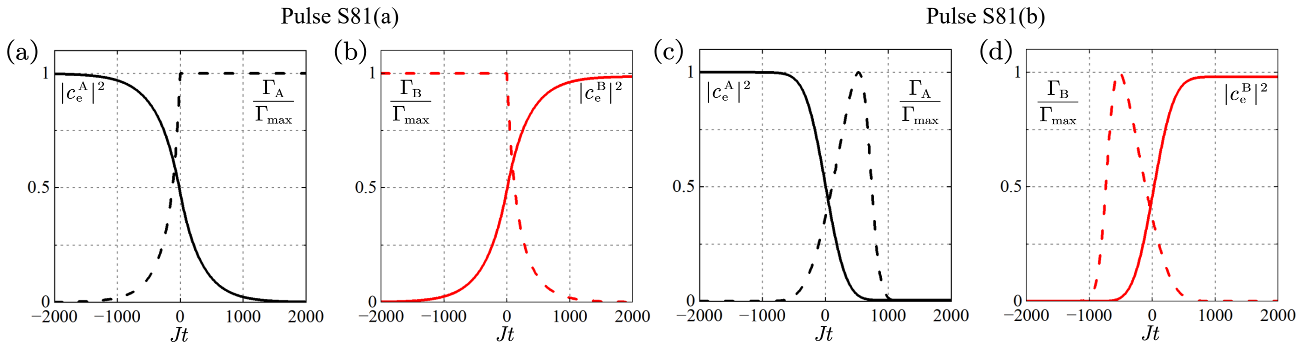

Figure S10. **Two-excitation transfer process between two GEPs.** The solid curves are the excitation probabilities of GEPs A and B. The dashed curves correspond to the modulating pulses, which are given by Eq. (S81a) for (a, b) and Eq. (S81b) for (c, d). The parameters are the same as in Fig. 2 in the main text.

Additionally, the initial and final state should also satisfy the boundary conditions

$$c_{\rm e}^{\rm A}(t_{\rm i}) = \left|c_{\rm e}^{\rm B}(t_{\rm f})\right| = 1, \qquad c_{\rm e}^{\rm A}(t_{\rm f}) = \left|c_{\rm e}^{\rm B}(t_{\rm i})\right| = 0, \tag{S80}$$

where $t_{\rm i}$ and $t_{\rm f}$ are the initial and final times, respectively. For convenience, we assume $t_{\rm i} = -t_{\rm f}$. As discussed in Ref. [S6], the following two types of control sequences can meet all above conditions:

$$\Gamma_{\rm A}(t) = \Gamma_{\rm B}(-t) = \begin{cases} \Gamma_0 \frac{e^{\Gamma_0 t}}{2-e^{\Gamma_0 t}}, & t<0, \\ \Gamma_0, & t \geq 0, \end{cases} \tag{S81a}$$

$$\Gamma_{\rm A}(t) = \Gamma_{\rm B}(-t) = \frac{\exp\left(-ct^2\right)}{\frac{1}{\Gamma_0} - \sqrt{\frac{\pi}{4c}}\mathrm{erf}(\sqrt{c}t)}, \tag{S81b}$$

where $c = 1.01 \times \Gamma^2(0)\pi/4$, and Γ_0 is given by Eq. (S45). Because $\Gamma_{\rm A,B} \propto g^4$, the modulating pulse $\Gamma_{\rm A,B}$ can be mapped as time-dependent coupling strengths $g_{\rm A,B}(t)$ according to Eq. (S76) and Eq. (S81). In Fig. S10, by fixing $c_{\rm g}(t) = 0$, we numerically plot the two-excitation energy transfer from GEP A to B under the control of the two pulse sequences in a finite waveguide with a length $N = 3000$. Note that the Stark shifts in Eq. (S76) are compensated by modulating the frequencies of two GEPs oppositely, i.e., $\omega_{\rm A(B)}(t) = 2\omega_{\rm e} - \sum_{i=1,2}\delta\omega_{{\rm A(B)},i}(t)$. We find that the transfer efficiency can reach $c_{\rm e}^{\rm B}(t_{\rm f}) \simeq 98\,\%$, which enables a high-fidelity entangled-state transfer between two GEPs.

Supplementary Note 4. FROM DOUBLON TO TRIPLON, AND FURTHER TO GROUPS OF $\mathcal{N}$ CORRELATED PHOTONS

Above we have discussed nonlinear chiral quantum optics with doublons. Note that in this nonlinear waveguide, states with $\mathcal{N}$ correlated photons, beyond pairs, also exist. The energy spectrum of the waveguide in the three-photon subspace is shown in Fig. S11(a). There, new three-photon bound states, referred to as "triplons", emerge between two- and three-photon scattering states. Now we show that unidirectional routing of "triplons" is also possible in our proposal. As depicted in Fig. 1 of the main text, three GEs are assumed to interact with the waveguide with $d = 1$ and $D = 0$. Their total frequency $3w_{\rm e}$ lies in the triplon spectrum [see Fig. S11(a)]. There are three coupling phases $\Phi_i^{\rm e}$ $(i = 1, 2, 3)$, indicating that the interference channels are much more complex than those of the doublons. In Fig. 5 of the main text, we assume that the coupling phase differences are identical, i.e., $\Phi_i^{\rm e} = \Phi_{\rm t}^{\rm e}$, and numerically search for the optimal point for directional emission of triplons, which is found at $\Phi_{\rm t}^{\rm e} = \pm 0.18\pi$.

To verify that triplons can mediate quantum information transfer between remote nodes without information back flow, we consider a minimal setup with two nodes A and B, each of which contains three GEs. The coupling phases of all GEs are set at the optimal chiral point $\Phi_{\rm t}^{\rm e} = 0.18\pi$. The tripartite GEs in node A (B) are initially in their excited (ground) states, and their evolutions are plotted in Fig. S11(b) by considering a finite waveguide with $N = 3000$. We find that the three correlated photons emitted by node A are absorbed by node B without being scattered back,

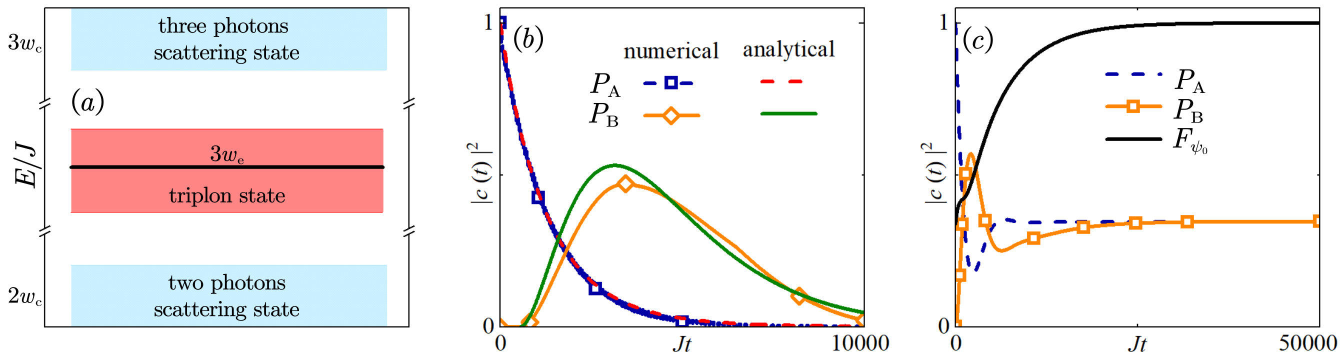

Figure S11. **Cascaded system for triplon.** (a) The total frequency of three GEs, $3\omega_e$ (black solid line), is set to be within the triplon spectrum. (b) Given that $\Phi_t^e = \pm 0.18\pi$, the time evolutions of the occupation probabilities in the cascaded system mediated by triplons. The probabilities of the three GEs in node A/B simultaneously being excited are denoted as $P_{A/B} = |c_e^{A/B}(t)|^2$. At $t = 0$, we set $|c_e^A(t)|^2 = 1$ and $|c_e^B(t)|^2 = 0$. (c) Time evolution of the fidelity F_{ψ_0} for the six-body entangled states (black curve), $|c_e^A(t)|^2$ (dashed blue curve), and $|c_e^B(t)|^2$ (orange curve with squares) in the presence of the parametric drive Ω_d.

and therefore, node A will not be re-excited. In this cascaded quantum system with interactions mediated by three correlated photons, the joint-quantum-jump operators are $S_\alpha^- = \sigma_{\alpha 1}^- \sigma_{\alpha 2}^- \sigma_{\alpha 3}^-$ ($\alpha = \mathrm{A, B}$). The unidirectional decay rate Γ_+ is obtained via exponential fitting of the evolution curve for P_A. Then, We can obtain the nonlinear cascaded master equation for triplons, whose evolution is shown in Fig. S11(b); it matches well with the results obtained by considering a finite waveguide.

We consider that the three GEs in the two remote nodes are pumped in the form of three-photon parametric down-conversion processes, i.e.,

$$H_{\text{pump}} = \Omega_d \sum_{\alpha = A,B} \sigma_{\alpha 1}^- \sigma_{\alpha 2}^- \sigma_{\alpha 3}^- + \text{H.c.} \tag{S82}$$

Such a nonlinear pump has been realized, for example, in circuit-QED platforms [S26]. Similar to discussions in Fig. S8(c), the dark state for this driven-dissipative cascaded system is

$$|\psi_0\rangle = |g\rangle^{\otimes 2\mathcal{N}} + i\frac{2\sqrt{2}\Omega_d}{\Gamma_+}|S\rangle, \qquad |S\rangle = \frac{|g\rangle^{\otimes \mathcal{N}} \otimes |e\rangle^{\otimes \mathcal{N}} - |e\rangle^{\otimes \mathcal{N}} \otimes |g\rangle^{\otimes \mathcal{N}}}{\sqrt{2}}, \quad \mathcal{N} = 3. \tag{S83}$$

In the limit $\Omega_d \gg \Gamma_+$, the dark state is approximately $|\psi_0\rangle \simeq |S\rangle$, which is a six-partite maximally entangled state for two remote nodes. Figure S11(c) shows that the dark-state fidelity F_{ψ_0} asymptotically approaches 1 in the steady state.

All the above results indicate that the groups of $\mathcal{N}$ correlated photons in this nonlinear waveguide can be exploited as "correlated flying qubits" for harnessing many-body states among remote quantum nodes. The detailed discussion on generalized cascaded quantum networks can be found in the main text.

Supplementary Note 5. SUPPLEMENTARY REFERENCES

Supplementary Reference

[S1] R. Piil and K. Mølmer, Tunneling couplings in discrete lattices, single-particle band structure, and eigenstates of interacting atom pairs, Phys. Rev. A **76**, 023607 (2007).

[S2] Z. Wang, T. Jaako, P. Kirton, and P. Rabl, Supercorrelated Radiance in Nonlinear Photonic Waveguides, Phys. Rev. Lett. **124**, 213601 (2020).

[S3] M. Valiente and D. Petrosyan, Two-particle states in the hubbard model, Journal of Physics B: Atomic, Molecular and Optical Physics **41**, 161002 (2008).

[S4] K. Stannigel, P. Rabl, A. S. Sørensen, P. Zoller, and M. D. Lukin, Optomechanical Transducers for Long-Distance Quantum Communication, Phys. Rev. Lett. **105**, 220501 (2010).

[S5] K. Stannigel, P. Rabl, A. S. Sørensen, M. D. Lukin, and P. Zoller, Optomechanical transducers for quantum-information processing, Phys. Rev. A **84**, 042341 (2011).

[S6] K. Stannigel, P. Rabl, and P. Zoller, Driven-dissipative preparation of entangled states in cascaded quantum-optical networks, New J. Phys. **14**, 063014 (2012).

[S7] X. Gu, A. F. Kockum, A. Miranowicz, Y.-X. Liu, and F. Nori, Microwave photonics with superconducting quantum circuits, Phys. Rep. **718-719**, 1 (2017).

[S8] P. Krantz, M. Kjaergaard, F. Yan, T. P. Orlando, S. Gustavsson, and W. D. Oliver, A quantum engineer's guide to superconducting qubits, Appl. Phys. Rev. **6**, 021318 (2019).

[S9] A. Blais, A. L. Grimsmo, S. M. Girvin, and A. Wallraff, Circuit quantum electrodynamics, Rev. Mod. Phys. **93**, 025005 (2021).

[S10] B. Kannan, M. J. Ruckriegel, D. L. Campbell, A. Frisk Kockum, J. Braumüller, D. K. Kim, M. Kjaergaard, P. Krantz, A. Melville, B. M. Niedzielski, A. Vepsäläinen, R. Winik, J. L. Yoder, F. Nori, T. P. Orlando, S. Gustavsson, and W. D. Oliver, Waveguide quantum electrodynamics with superconducting artificial giant atoms, Nature **583**, 775 (2020).

[S11] A. M. Vadiraj, A. Ask, T. G. McConkey, I. Nsanzineza, C. W. S. Chang, A. F. Kockum, and C. M. Wilson, Engineering the level structure of a giant artificial atom in waveguide quantum electrodynamics, Phys. Rev. A **103**, 023710 (2021).

[S12] C. Joshi, F. Yang, and M. Mirhosseini, Resonance fluorescence of a chiral artificial atom, Phys. Rev. X **13**, 021039 (2023).

[S13] J. Koch, T. M. Yu, J. Gambetta, A. A. Houck, D. I. Schuster, J. Majer, A. Blais, M. H. Devoret, S. M. Girvin, and R. J. Schoelkopf, Charge-insensitive qubit design derived from the Cooper pair box, Phys. Rev. A **76**, 042319 (2007).

[S14] S. Hacohen-Gourgy, V. V. Ramasesh, C. De Grandi, I. Siddiqi, and S. M. Girvin, Cooling and autonomous feedback in a bose-hubbard chain with attractive interactions, Phys. Rev. Lett. **115**, 240501 (2015).

[S15] P. Roushan, C. Neill, J. Tangpanitanon, V. M. Bastidas, A. Megrant, R. Barends, Y. Chen, Z. Chen, B. Chiaro, A. Dunsworth, A. Fowler, B. Foxen, M. Giustina, E. Jeffrey, J. Kelly, E. Lucero, J. Mutus, M. Neeley, C. Quintana, D. Sank, A. Vainsencher, J. Wenner, T. White, H. Neven, D. G. Angelakis, and J. Martinis, Spectroscopic signatures of localization with interacting photons in superconducting qubits, Science **358**, 1175 (2017).

[S16] G. P. Fedorov, S. V. Remizov, D. S. Shapiro, W. V. Pogosov, E. Egorova, I. Tsitsilin, M. Andronik, A. A. Dobronosova, I. A. Rodionov, O. V. Astafiev, and A. V. Ustinov, Photon transport in a bose-hubbard chain of superconducting artificial atoms, Phys. Rev. Lett. **126**, 180503 (2021).

[S17] E. Kim, X. Zhang, V. S. Ferreira, J. Banker, J. K. Iverson, A. Sipahigil, M. Bello, A. González-Tudela, M. Mirhosseini, and O. Painter, Quantum electrodynamics in a topological waveguide, Phys. Rev. X **11**, 011015 (2021).

[S18] S. Krinner, N. Lacroix, A. Remm, A. Di Paolo, E. Genois, C. Leroux, C. Hellings, S. Lazar, F. Swiadek, J. Herrmann, G. J. Norris, C. K. Andersen, M. Müller, A. Blais, C. Eichler, and A. Wallraff, Realizing repeated quantum error correction in a distance-three surface code, Nature **605**, 669674 (2022).

[S19] A. P. M. Place, L. V. H. Rodgers, P. Mundada, B. M. Smitham, M. Fitzpatrick, Z. Leng, A. Premkumar, J. Bryon, A. Vrajitoarea, S. Sussman, G. Cheng, T. Madhavan, H. K. Babla, X. H. Le, Y. Gang, B. Jäck, A. Gyenis, N. Yao, R. J. Cava, N. P. de Leon, and A. A. Houck, New material platform for superconducting transmon qubits with coherence times exceeding 0.3 milliseconds, Nature Communications **12**, 10.1038/s41467-021-22030-5 (2021).

[S20] M. R. Geller, E. Donate, Y. Chen, M. T. Fang, N. Leung, C. Neill, P. Roushan, and J. M. Martinis, Tunable coupler for superconducting Xmon qubits: Perturbative nonlinear model, Phys. Rev. A **92**, 012320 (2015).

[S21] F. Wulschner, J. Goetz, F. R. Koessel, E. Hoffmann, A. Baust, P. Eder, M. Fischer, M. Haeberlein, M. J. Schwarz, M. Pernpeintner, E. Xie, L. Zhong, C. W. Zollitsch, B. Peropadre, J.-J. Garcia-Ripoll, E. Solano, K. G. Fedorov, E. P. Menzel, F. Deppe, A. Marx, and R. Gross, Tunable coupling of transmission-line microwave resonators mediated by an rf SQUID, EPJ Quantum Technol. **3**, 10 (2016).

[S22] J. I. Cirac, P. Zoller, H. J. Kimble, and H. Mabuchi, Quantum State Transfer and Entanglement Distribution among Distant Nodes in a Quantum Network, Phys. Rev. Lett. **78**, 3221 (1997).

[S23] B. Vermersch, P.-O. Guimond, H. Pichler, and P. Zoller, Quantum State Transfer via Noisy Photonic and Phononic Waveguides, Phys. Rev. Lett. **118**, 133601 (2017).

[S24] Z.-L. Xiang, M. Zhang, L. Jiang, and P. Rabl, Intracity Quantum Communication via Thermal Microwave Networks, Phys. Rev. X **7**, 011035 (2017).

[S25] X. Wang and H.-R. Li, Chiral quantum network with giant atoms, Quantum Sci. Technol. **7**, 035007 (2022).

[S26] C. W. S. Chang, C. Sabín, P. Forn-Díaz, F. Quijandría, A. M. Vadiraj, I. Nsanzineza, G. Johansson, and C. M. Wilson, Observation of three-photon spontaneous parametric down-conversion in a superconducting parametric cavity, Phys. Rev. X **10**, 011011 (2020).